Applied Mathematical Modelling 111 (2022) 836–861

Contents lists available at ScienceDirect

Applied Mathematical Modelling

journal homepage: www.elsevier.com/locate/apm

Fully coupled interface-tracking model for axisymmetric ferrohydrodynamic flows

Á. Romero-Calvo[a,*], M.A. Herrada[b], G. Cano-Gómez[c], H. Schaub[a]

[a] *Department of Aerospace Engineering Sciences, University of Colorado Boulder, CO, United States*
[b] *Departamento de Ingeniería Aeroespacial y Mecánica de Fluidos, Universidad de Sevilla, Avenida de los Descubrimientos s/n, Sevilla, 41092, Spain*
[c] *Departamento de Física Aplicada III, Universidad de Sevilla, Avenida de los Descubrimientos s/n, Sevilla, 41092, Spain*

ARTICLE INFO

Article history:
Received 10 October 2021
Revised 7 June 2022
Accepted 30 June 2022
Available online 7 July 2022

Keywords:
Ferrohydrodynamics
Multiphase flows
Microgravity
Sloshing
Space technology

ABSTRACT

A coupled ferrohydrodynamic interface-tracking model is introduced for the analysis of the equilibrium, linear stability, and modal response of magnetic liquid interfaces in surface tension-dominated axisymmetric multiphase flows. The incompressible viscous mass and momentum balances are solved together with the steady-state Maxwell equations by following a monolithic solution scheme. The method is fully implicit, allowing to reach a steady-state solution in a single time step. In addition, the time-dependent evolution of the interface subject to variable external inputs can also be simulated. The geometry is particularized for the study of the free surface oscillations of a ferrofluid in a cylindrical tank under the influence of an inhomogeneous magnetic field in microgravity. Five regions are used to discretize the simulation domain, which combines analytical and elliptic mappings. Magnetic-field-free results are validated by the literature. The modal response of the fluid-magnetic system agrees with measurements from the European Space Agency (ESA) *Drop Your Thesis!* 2017 *The Ferros* experiment and improves previous quasi-analytical estimations. This new framework of analysis can be applied to the study of a wide variety of microfluidic and low-gravity fluid systems.

1. Introduction

Several systems in physics and engineering employ highly susceptible magnetic liquids to touchlessly control the behavior of multiphase flows. This intersection is particularly prolific in milli/microfluidic and space applications, where surface tension overcomes gravity and only a limited range of actuation mechanisms is available. Magnetic liquids have been employed in bubble and droplet studies [1–3], T-junctions [4–6], mass transfer [7–11], thermomagnetic convection [12,13], micropropulsion systems [14,15], or energy harvesters [16–18], among others. These works are characterized by the strong coupling between fluid and magnetic problems, that forces their simultaneous (or, at least, iterative) solution. However, the relative immaturity of ferrohydrodynamic simulation frameworks and a certain misunderstanding on how such systems should be treated commonly leads to inappropriate modeling approaches, as discussed in Ref. [3].

Recent works have addressed the numerical simulation of coupled ferrohydrodynamic problems. A classification of these efforts may consider two key characteristics: solution procedure and multiphase flow modeling approach. In the first category, and excluding implementations where the fluid-magnetic coupling is ignored or heavily simplified, *partitioned* schemes

---

[*] Corresponding author.
E-mail address: alvaro.romerocalvo@colorado.edu (Á. Romero-Calvo).

https://doi.org/10.1016/j.apm.2022.06.046

that iteratively solve the fluid-magnetic equations seems predominant [19–25]. In contrast, *monolithic* approaches solve all equations simultaneously within a global nonlinear system and have also been implemented using the finite elements method [26–28]. Although monolithic approaches deal with the inversion of a large Jacobian, require more memory, and renounce to the modularity of partitioned schemes, they are also more robust and generally more computationally efficient than iterative implementations, particularly for complex multiphysics problems [29–32]. From the multiphase flow modeling perspective, the Lattice Boltzmann [23,25,33,34], level set [24], phase field [35], and volume of fluid methods [20,28], or a combination of the previous [21] have been employed. The last three can be categorized as interface-capturing, meaning that an auxiliary function is introduced in a fixed spatial domain to determine the location of the interface. Although their versatility has made them extremely popular in the multiphase flow community, interface-capturing methods face significant challenges when dealing with the formulation and implementation of surface tension [36]. This includes the mitigation of numerical diffusion at the interface, the computation of surface normals and curvatures, or the imposition of a discrete balance of surface tension and pressure gradient terms [37]. In contrast, interface-tracking methods employ meshes that follow the fluid surface by advecting with the flow a discrete set of points distributed along the interface. This approach avoids numerical diffusion, provides a seamless implementation of surface tension forces, and leads to simpler boundary conditions, which makes it particularly appropriate for capillary and low-gravity fluid problems. However, the transformation employed to transition from the uniform computational domain to the deformed mesh complicates the final expression of the governing equations and limits their applicability to relatively simple geometries [38].

Interface-tracking methods for coupled, capillary ferrohydrodynamic systems remain, to the best knowledge of the authors, completely unexplored. Their development would be highly desirable for the study of a wide variety of fundamental and applied problems, ranging from bubble and droplet studies to microfluidic and low-gravity systems. This paper extends the interface-tracking framework introduced in Ref. [38] to address for the first time the equilibrium, linear stability, modal response, and time-dependent deformation of ferrohydrodynamic capillary liquid interfaces. A robust and numerically stable implementation is achieved by employing a fully implicit monolithic approach that solves both problems with essentially the same code. Its implicit nature allows using arbitrarily large time steps on each Newton-Raphson iteration. Symbolic functions and collocation matrices are employed to evaluate the Jacobian of the discretized system of equations and take advantage of the sparsity of the resulting matrix, leading to significant gains in flexibility and computational efficiency with respect to previous approaches, as demonstrated in Ref. [38].

One of the unique capabilities of the model is its ability to easily compute the modal shapes and frequencies of ferrohydrodynamic interfaces. The validation of this feature is complicated by the fact that previous experiments were mostly concerned with the equilibrium and dynamic evolution of ferrofluid interfaces rather than their modal response. An exception is the European Space Agency (ESA) *Drop Your Thesis!* 2017 *The Ferros* project, that studied the axisymmetric sloshing of water-based ferrofluids when subjected to an inhomogeneous magnetic field in microgravity [39–41]. Although the axisymmetric and lateral sloshing of ferrofluids were also studied during the United Nations Office for Outer Space Affairs (UNOOSA) DropTES 2019 experiment *StELIUM* [42–44], statistical significance was not achieved for the axisymmetric modes [45]. Therefore, the configuration of the *Drop Your Thesis!* 2017 experiment is adopted in this work.

From a technical perspective, the ESA *Drop Your Thesis!* 2017 experiment *The Ferros* was conceived to test new magnetic propellant management devices for in-space propulsion [41]. Propellant sloshing is one of the paramount low-gravity fluid dynamic problems due to its inherent complexity and impact on the operation of space vehicles [46–48]. In an attempt to address this problem, Papell invented ferrofluids, defined as colloidal suspensions of magnetic nanoparticles in a carrier liquid, in the early 1960s [49]. Although the idea of using magnetic liquids for slosh control remained dormant for decades, it has been revisited several times since the late 1990s [50–59]. A quasi-analytical model was recently introduced to study the equilibrium and modal response of ferrofluid interfaces in microgravity [22]. The model has been shown to offer an excellent estimation of the lateral modal frequencies in the aforementioned UNOOSA DropTES 2019 campaign [45], but over-predicted the axisymmetric sloshing frequencies of the ESA Drop Your Thesis! 2017 experiment [41]. An additional (technical) motivation for this work is thus to shed light on this disagreement and develop a tool that provides the equilibrium, global stability, modal response, and time-dependent evolution of the capillary ferrohydrodynamic interfaces that may find application in space propulsion.

In this paper, the problem under study is formulated in Section 2, the numerical method is described in Section 3, and numerical results are discussed and compared with the literature in Section 4.

2. Problem formulation

2.1. Problem geometry

The system under analysis, represented in Fig. 1, consists of a partially filled cylindrical tank subject to an inhomogeneous axisymmetric magnetic field. Such field is imposed by either a coil or a magnet. The tank has radius R, height h_B, and holds a volume V of an incompressible magnetic liquid with density ρ, specific volume $\nu = \rho^{-1}$, shear coefficient of viscosity η, and surface tension σ at temperature T. The static contact angle between the liquid and the wall is θ_c. The free space is filled by a non-reactive inviscid gas at pressure p_g. A vertical inertial acceleration g is also applied to the tank.

The system is studied by means of a coupled ferrohydrodynamic model that is able to compute the (i) axisymmetric meniscus, (ii) global stability properties, (iii) axisymmetric oscillation modes, and (iv) time-dependent evolution of the free

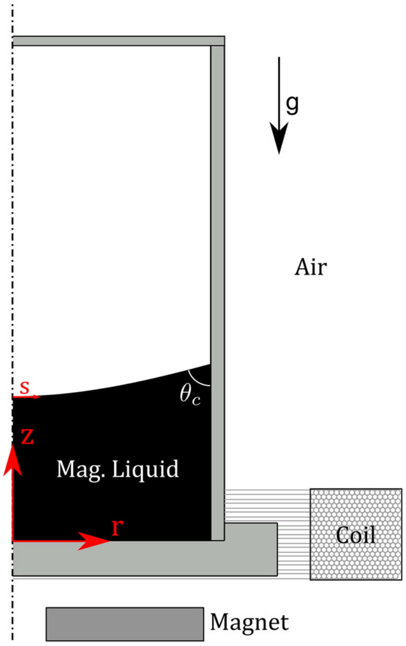

Fig. 1. System under analysis.

liquid surface. Although this framework of analysis can be applied to a variety problems, the experimental setup implemented for the ESA *Drop Your Thesis!* 2017 *The Ferros* project [39–41] is chosen for verification and validation. The geometry is particularized in Section 4.1.

2.2. Stress tensor and force distributions

The magnetodynamic state of an incompressible continuous medium is described by means of the viscous Maxwell stress tensor, given by [60–63]

$$\mathcal{T} = \mathcal{T}_p + \mathcal{T}_\nu + \mathcal{T}_m, \tag{1}$$

where the pressure, viscous, and magnetic terms are $\mathcal{T}_p = -p^*\,\mathcal{I}$,

$$\mathcal{T}_\nu = \eta\left[\nabla\boldsymbol{v} + (\nabla\boldsymbol{v})^T\right], \tag{2b}$$

$$\mathcal{T}_m = -\frac{\mu_0}{2}H^2\mathcal{I} + \boldsymbol{BH}, \tag{2c}$$

and where

$$p^* = p(\nu, T) + \mu_0\int_0^H \frac{\partial}{\partial\nu}[\nu M]dH' \tag{3}$$

is the *composite pressure*, which includes hydrostatic $p(\nu, T)$ and magnetopolarization terms. In these expressions, $\boldsymbol{B} = \mu_0(\boldsymbol{H}+\boldsymbol{M})$, $\boldsymbol{H}$, and $\boldsymbol{M}$ are the flux density, magnetic, and magnetization fields, μ_0 is the permeability of vacuum, $\mathcal{I} = \delta_{ij}\boldsymbol{e}_i\boldsymbol{e}_j$ is the unit dyadic in the Cartesian $\boldsymbol{e}_i$ reference system, and $\boldsymbol{v}$ is the fluid velocity. For symmetrical fluids, the magnetization and magnetic fields are aligned and follow the relation

$$\boldsymbol{M} = \chi^{\mathrm{vol}}(H)\boldsymbol{H}, \tag{4}$$

with $\chi^{\mathrm{vol}}(H)$ being the volume magnetic susceptibility. Alternating magnetic fields at sufficiently high frequencies or fluids with very large vortex viscosity values may render Eq. (4) inappropriate due to the transient misalignment between $\boldsymbol{M}$ and $\boldsymbol{H}$ [64]. However, as shown in Section 4.3, this is not a concern for the problems considered in this work.

The forces per unit volume exerted on the medium in the absence of electric fields are computed as the divergence of the stress tensor given by Eq. (1), resulting in [63]

$$\boldsymbol{f} = \boldsymbol{f}_p + \boldsymbol{f}_\nu + \boldsymbol{f}_m, \tag{5}$$

with

$$\boldsymbol{f}_p = \nabla\cdot\mathcal{T}_p = -\nabla p^*, \tag{6a}$$

$$\boldsymbol{f}_\nu = \nabla \cdot \mathcal{T}_\nu = \nabla \cdot \left\{\eta\left[\nabla\boldsymbol{v} + (\nabla\boldsymbol{v})^T\right]\right\}, \tag{6b}$$

$$\boldsymbol{f}_m = \nabla \cdot \mathcal{T}_m = \mu_0 M \nabla H = \mu_0 (\boldsymbol{M} \cdot \nabla)\boldsymbol{H}. \tag{6c}$$

If the viscosity coefficient is constant, the viscous term reduces to

$$\boldsymbol{f}_\nu = \eta \nabla^2 \boldsymbol{v}. \tag{7}$$

Surface forces appear in the gas-liquid interface as a consequence of the discontinuity in the stress tensor. Those forces are balanced according to the *ferrohydrodynamic incompressible viscous boundary condition*. Assuming a contact between a ferrofluid and a non-magnetic, inviscid gas, the condition is expressed in normal (n) and tangential (t) components as [63]

$$n: \quad p^* - 2\eta \frac{\partial v_n}{\partial x_n} + p_n - p_g = 2\sigma \mathcal{H}, \tag{8a}$$

$$t: \quad \eta\left(\frac{\partial v_n}{\partial x_t} + \frac{\partial v_t}{\partial x_n}\right) = 0, \tag{8b}$$

with $\boldsymbol{n}$ being the external normal vector, $p_n = \mu_0 M_n^2/2$ the *magnetic normal traction*, $\mathcal{H}$ the mean curvature of the interface, v_n and v_t the normal and tangential velocity components, and x_n and x_t the distances along the normal and tangential directions, respectively. Further details on the derivation of the magnetic system of forces can be found in the Appendix A.

2.3. Governing equations for a magnetic, viscous, incompressible fluid

The ferrohydrodynamic mass and momentum conservation equations that derive from the stress tensor in Eq. (1) are [63]

$$\nabla \cdot \boldsymbol{v} = 0, \tag{9a}$$

$$\rho \frac{D\boldsymbol{v}}{Dt} = \rho\boldsymbol{g} + \boldsymbol{f}_p + \boldsymbol{f}_\nu + \boldsymbol{f}_m, \tag{9b}$$

with D denoting the material derivative, and t the time. This system of equations is subject to an appropriate set of boundary conditions. Particular attention should be payed to those described by Eq. (8), which exhibit the fluid-magnetic coupling through p_n.

Applications involving unequilibrated ferrofluid solutions, for which $\boldsymbol{M} \times \boldsymbol{H} \neq \boldsymbol{0}$, should also incorporate the effects resulting from particle rotation. An additional term is then added to the viscous stress tensor $\mathcal{T}_\nu$, and the angular momentum and magnetic relaxation equations also have to be taken into account [62,63]. As previously noted, symmetrical fluids are considered in this paper, and therefore $\boldsymbol{M} \times \boldsymbol{H} = \boldsymbol{0}$.

The terms $\boldsymbol{f}_p$ and $\boldsymbol{f}_m$ are defined by the fields $\boldsymbol{H}$, $\boldsymbol{B}$, and $\boldsymbol{M}$, which have to be computed at each time step by solving the magnetic problem. Assuming a static magnetic configuration without surface currents and electric fields, the magnetostatic equations that determine such fields are [65]

$$\nabla \cdot \boldsymbol{B} = 0, \tag{10a}$$

$$\nabla \times \boldsymbol{H} = \boldsymbol{J}_e, \tag{10b}$$

where $\boldsymbol{J}_e$ is the volume density of electric current. The magnetic boundary conditions are

$$\boldsymbol{n} \cdot [\boldsymbol{B}\,] = 0, \tag{11a}$$

$$\boldsymbol{n} \times [\boldsymbol{H}\,] = \boldsymbol{K}_e, \tag{11b}$$

with $\boldsymbol{K}_e$ denoting the electric surface currents, and [-] the difference across the interface. Although surface currents are not considered in this work, they will play a relevant role in the virtual magnet substitution procedure described in Section 3.3.1. Therefore, the normal component of $\boldsymbol{B}$ and the tangential component of $\boldsymbol{H}$ are continuous across the interfaces.

3. Numerical method

The theoretical framework described in Section 2 is particularized for the cylindrical reference system $\{\boldsymbol{e}_r, \boldsymbol{e}_\phi, \boldsymbol{e}_z\}$ depicted in Fig. 1. The equations presented in this section are therefore the ones solved by the numerical framework. Five regions and their corresponding interfaces conform the simulation domain, as shown in Fig. 2: A (liquid), B (air inside the container), C (air over the container), D (air below the container), and E (surrounding air). The subdivision between regions B and C is not strictly necessary; however, adding a buffer area on top of B allows expanding the simulation domain while easily controlling the mesh density. The magnetic source (e.g. a coil or magnet) is included in E as a subdomain $\mathrm{E_c}$.

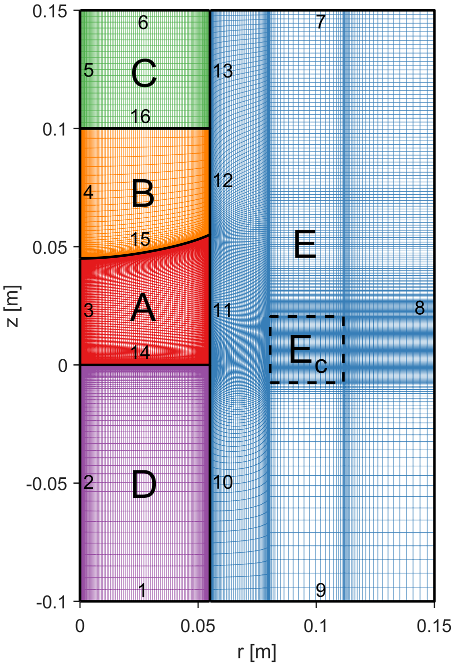

Fig. 2. Numerical simulation domain with mapped regions and interfaces. The dashed rectangle denotes the virtual coil domain.

3.1. Axisymmetric Navier-Stokes equations

The mass and momentum conservation equations defined by Eq. (9) should be expressed in the cylindrical reference system after considering the axisymmetry of the problem. This results in

$$\frac{\partial(ru)}{\partial r}+\frac{\partial(rw)}{\partial z}=0, \tag{12a}$$

$$\rho\left(\frac{\partial u}{\partial t}+u\frac{\partial u}{\partial r}+w\frac{\partial u}{\partial z}\right)=-\frac{\partial p^*}{\partial r}+\eta\left(\frac{\partial^2 u}{\partial r^2}+\frac{\partial(u/r)}{\partial r}+\frac{\partial^2 u}{\partial z^2}\right)+\mu_0\left(M_r\frac{\partial H_r}{\partial r}+M_z\frac{\partial H_r}{\partial z}\right), \tag{12b}$$

$$\rho\left(\frac{\partial w}{\partial t}+u\frac{\partial w}{\partial r}+w\frac{\partial w}{\partial z}\right)=\rho g-\frac{\partial p^*}{\partial z}+\eta\left(\frac{\partial^2 w}{\partial r^2}+\frac{1}{r}\frac{\partial w}{\partial r}+\frac{\partial^2 w}{\partial z^2}\right)+\mu_0\left(M_r\frac{\partial H_z}{\partial r}+M_z\frac{\partial H_z}{\partial z}\right), \tag{12c}$$

where r (z) is the radial (axial) coordinate, and u (w) is the radial (axial) velocity component. The axisymmetry of the magnetic problem is taken into account in the previous expressions, so that $\boldsymbol{J}_e$ has only azimuthal components, and $\boldsymbol{M}$ and $\boldsymbol{H}$ lack from them, resulting in $\boldsymbol{H}=H_r\boldsymbol{e}_r+H_z\boldsymbol{e}_z$, and $\boldsymbol{M}=M_r\boldsymbol{e}_r+M_z\boldsymbol{e}_z$. For practical reasons, vertically magnetized magnets will be considered.

3.2. Magnetic potentials for axisymmetric problem

Equations (10a) and (10b) are rewritten as a function of $\boldsymbol{H}$, resulting in

$$\nabla\cdot\boldsymbol{H}=-\nabla\cdot\boldsymbol{M}, \tag{13a}$$

$$\nabla\times\boldsymbol{H}=\boldsymbol{J}_e. \tag{13b}$$

Therefore, $\boldsymbol{H}$ has scalar sources in the magnetized regions and vector sources in the coil. According to Helmholtz's theorem, $\boldsymbol{H}$ can be expressed in terms of scalar and vector magnetic potentials. Taking into account the axisymmetry of the problem,

$$H_r=-\frac{1}{r}\frac{\partial\Psi}{\partial z}-\frac{\partial\Phi}{\partial r},\quad H_z=\frac{1}{r}\frac{\partial\Psi}{\partial r}-\frac{\partial\Phi}{\partial z}, \tag{14}$$

where Φ is the scalar potential generated by scalar sources and the stream-like function $\Psi=rA_\phi(r,z)/\mu_0$ is directly related to the azimuthal component $A_\phi(r,z)$ of the vector magnetic potential created by the electric current. The magnetic problem is then formulated and solved in terms of Φ and Ψ after noting that

$$\nabla \cdot \boldsymbol{H} = -\left[\frac{\partial^2 \Phi}{\partial z^2} + \frac{\partial^2 \Phi}{\partial r^2} + \frac{1}{r}\frac{\partial \Phi}{\partial r}\right], \tag{15}$$

$$\nabla \times \boldsymbol{H} = -\frac{1}{r}\left[\frac{\partial^2 \Psi}{\partial r^2} + \frac{\partial^2 \Psi}{\partial z^2} - \frac{1}{r}\frac{\partial \Psi}{\partial r}\right]\boldsymbol{e}_\phi. \tag{16}$$

In the domain A, $\boldsymbol{M} = \chi^{\mathrm{vol}}(H)\boldsymbol{H}$ and Eq. (13a) becomes

$$\frac{\partial^2 \Phi}{\partial z^2} + \frac{\partial^2 \Phi}{\partial r^2} + \frac{1}{r}\frac{\partial \Phi}{\partial r} = \frac{1}{1+\chi^{\mathrm{vol}}(H)}\left(H_r\frac{\partial \chi^{\mathrm{vol}}}{\partial r} + H_z\frac{\partial \chi^{\mathrm{vol}}}{\partial z}\right), \tag{17}$$

where χ^{vol} also depends on Ψ and Φ through the magnetization law

$$\chi^{\mathrm{vol}}(H) = \frac{2a_M}{\pi H}\arctan(c_M H) + \frac{2b_M}{\pi H}\arctan(d_M H) + e_M, \tag{18}$$

with a_M, b_M, c_M, d_M, and e_M being a set of fitting parameters [41]. For domains B-E, Eq. (13a) is simplified to $\nabla \cdot \boldsymbol{H} = 0$ due to the absence of inhomogeneous magnetization fields. It should be noted, however, that magnets may be considered in the subdomain $\mathrm{E_c}$. When such subdomain is occupied by a coil,

$$\boldsymbol{J}_e = \frac{NI}{S_c}\boldsymbol{e}_\phi, \tag{19}$$

with N being the number of wire turns, I the current flowing through each of them, and S_c the cross section of the coil. Consequently, Eq. (13b) adopts the form

$$-\frac{1}{r}\left[\frac{\partial^2 \Psi}{\partial r^2} + \frac{\partial^2 \Psi}{\partial z^2} - \frac{1}{r}\frac{\partial \Psi}{\partial r}\right] = \frac{NI}{S_c}. \tag{20}$$

For domains A–D (and E, when $\mathrm{E_c}$ is occupied by a magnet), $\boldsymbol{J}_e = \boldsymbol{0}$, and the previous expression simplifies to $\nabla \times \boldsymbol{H} = \boldsymbol{0}$. If a magnet with uniform, vertical magnetization field is considered in $\mathrm{E_c}$, the condition $\boldsymbol{M} = M_m\boldsymbol{e}_z$ is imposed at such region and the stream-like function has trivial solution $\Psi = 0$.

3.3. Boundary conditions

An axisymmetric boundary condition is applied at $r = 0$ for both fluid and magnetic problems, while the wall-liquid interaction is described by the non-penetration and no-slip boundary conditions. This results in

$$3:\ \ u = 0, \quad \frac{\partial w}{\partial r} = 0, \tag{21a}$$

$$11:\ \ u = w = 0, \tag{21b}$$

$$14:\ \ u = w = 0. \tag{21c}$$

The interfacial conditions described by Eq. (8) are particularized at the free fluid surface 15 by following a parametrization of the form $z_{\mathrm{in}} = G(s,t)$ and $r_{\mathrm{in}} = F(s,t)$, resulting in the normal balance

$$p^* + p_n - p_0 = \frac{\sigma}{F}\left(\frac{\partial F}{\partial s}\right)^{-1}\frac{\partial}{\partial s}\left[\frac{F\frac{\partial G}{\partial s}}{\sqrt{\left(\frac{\partial F}{\partial s}\right)^2 + \left(\frac{\partial G}{\partial s}\right)^2}}\right] + 2\eta\frac{\frac{\partial u}{\partial r}\left(\frac{\partial G}{\partial s}\right)^2 + \frac{\partial w}{\partial z}\left(\frac{\partial F}{\partial s}\right)^2 - \left(\frac{\partial w}{\partial r} + \frac{\partial u}{\partial z}\right)\frac{\partial F}{\partial s}\frac{\partial G}{\partial s}}{\left(\frac{\partial G}{\partial s}\right)^2 + \left(\frac{\partial F}{\partial s}\right)^2}, \tag{22a}$$

tangential balance

$$\frac{\left[\left(\frac{\partial G}{\partial s}\right)^2 - \left(\frac{\partial F}{\partial s}\right)^2\right]\left(\frac{\partial w}{\partial r} + \frac{\partial u}{\partial z}\right) + 2\frac{\partial F}{\partial s}\frac{\partial G}{\partial s}\left(\frac{\partial u}{\partial r} - \frac{\partial w}{\partial z}\right)}{\left(\frac{\partial F}{\partial s}\right)^2 + \left(\frac{\partial G}{\partial s}\right)^2} = 0, \tag{22b}$$

and the kinematic and geometric compatibility equations

$$\left(u - \frac{\partial F}{\partial t}\right)\frac{\partial G}{\partial s} - \left(w - \frac{\partial G}{\partial t}\right)\frac{\partial F}{\partial s} = 0, \tag{22c}$$

$$\frac{\partial G}{\partial s}\frac{\partial^2 G}{\partial s^2} + \frac{\partial F}{\partial s}\frac{\partial^2 F}{\partial s^2} = 0, \tag{22d}$$

where s is the arc length coordinate along the interface. The contact angle θ_c is imposed at the wall ($s = 1$) through

$$\frac{\partial F}{\partial s}\tan\left(\frac{\pi}{2}-\theta_c\right)+\frac{\partial G}{\partial s}=0, \quad \text{and} \quad F=R. \tag{22e}$$

The magnetic boundary conditions derive from Eq. (11) after considering the axisymmetry of the problem and noting that the liquid is magnetized. Two conditions can be imposed per block and boundary, which leads to four equations per internal connection and two per external boundary. The internal boundary conditions are

$$11,14,15: \quad \Psi_1=\Psi_2, \quad \Phi_1=\Phi_2, \tag{23a}$$

$$H_{t,1}=H_{t,2}, \quad B_{n,1}=B_{n,2}, \tag{23b}$$

$$10,12,13: \quad \Psi_1=\Psi_2, \quad \Phi_1=\Phi_2, \tag{23c}$$

$$\frac{\partial \Psi_1}{\partial r}=\frac{\partial \Psi_2}{\partial r}, \quad \frac{\partial \Phi_1}{\partial r}=\frac{\partial \Phi_2}{\partial r}, \tag{23d}$$

$$16: \quad \Psi_1=\Psi_2, \quad \Phi_1=\Phi_2, \tag{23e}$$

$$\frac{\partial \Psi_1}{\partial z}=\frac{\partial \Psi_2}{\partial z}, \quad \frac{\partial \Phi_1}{\partial z}=\frac{\partial \Phi_2}{\partial z}, \tag{23f}$$

where, in order to ensure the continuity of the magnetic field at 10, 12, 13 and 16, the continuity of the potentials Ψ and Φ and their derivatives across the internal boundary are imposed. The continuity of the derivative along the boundary is implicitly enforced by the continuity of the potential. In the fluid-air interfaces 11, 14, and 15, H_t and B_n are expressed as a function of the potentials and the normal and tangent vectors, and the analytical expressions are equaled at both side of the interface. It should be noted that the continuity of the potentials across a magnetized domain or a coil is a consequence of the magnetic field formulation shown in Eq. (14). The opposite would lead to a singularity (i.e. a nonphysical solution). This also motivates the modeling of such magnetic sources as subdomains of region E, named E_c, where either the source term $\boldsymbol{J}_e$ is considered in Eq. (20) (and not in the rest of the domain), or a vertical magnetization value is imposed.

Two conditions are applied to the external contours. In the axis,

$$2-5: \quad \Psi=0, \quad \frac{\partial \Phi}{\partial r}=0, \tag{24}$$

which results in $H_r = 0$ (see Eq. (14)) and imposes a reference value for Ψ. The potential Ψ is truncated at the external contours (1,6-9) by imposing its analytical solution, which can be easily found as the superposition of magnetic potentials induced by virtual circular loops located in the region of interest. This can be expressed as [65]

$$\Psi(r,z)|_{1,6-9}\approx\frac{NI}{N_iN_j}\sum_{i=1}^{N_i}\sum_{j=1}^{N_j}\Psi_{i,j}(r,z)|_{1,6-9}, \tag{25a}$$

$$\Psi_{i,j}(r,z)|_{1,6-9}=\frac{1}{\pi k_{i,j}}\sqrt{r_ir}\left[\left(1-\frac{k_{i,j}^2}{2}\right)K(k_{i,j})-E(k_{i,j})\right], \tag{25b}$$

with N being the number of turns of the actual coil, I its current intensity, $k_{i,j}^2 = 4r_ir/\left[(r_i+r)^2+(z-z_j)^2\right]$ an intermediate parameter, r_i (z_j) the virtual loop radius (height), N_i (N_j) the number of virtual loops in the radial (vertical) direction, and $K(k)$ ($E(k)$) the complete elliptic integral of first (second) kind computed with Matlab's `ellipke` function. The potential is shown to converge with errors below 0.001% for $N_i = N_j = 15$, which are adopted for the analysis.

The sources of scalar potential Φ are the magnetically polarizable liquid in A and an hypothetical magnet in E_c. Its value at the external contour can be approximated by the contribution of the dipole terms of the magnet and magnetized liquid, and so the condition

$$\Phi(r,z)|_{1,6-9}\approx\Phi^{\text{dip}}(r,z)|_{1,6-9} \tag{26a}$$

is imposed, with

$$\Phi^{\text{dip}}(r,z)|_{1,6-9}=\sum_{k=1}^{N_k}\frac{m_k}{4\pi}\frac{(z-z_k)}{[r^2+(z-z_k)^2]^{3/2}}\bigg|_{1,6-9}, \tag{26b}$$

where the N_k magnetized domains are characterized by the dipole moments $\boldsymbol{m}_k = m_k\boldsymbol{e}_z$ located at $\boldsymbol{r}_k = z_k\boldsymbol{e}_z$. The dipole associated with the magnet can be calculated beforehand, but the position and magnitude of the one deriving from the magnetized liquid needs to be computed by integrating $\boldsymbol{M}$ in the domain A. Although this Dirichlet boundary condition exhibits excellent numerical stability properties, a Neumann condition with higher spatial convergence rate may be imposed instead by considering the radial and axial derivatives of Φ. The unicity of the solution should then be imposed by setting the value of Φ in an arbitrary point of the external boundary. However, this implies that different conditions are applied along the same line, leading to slight numerical errors in the potential field.

It should be noted that, if the system only includes magnets and magnetized liquids, the boundary condition given by Eq. (25a) becomes unnecessary, since $\Psi_{1,6-9} = 0$. Similarly, it is possible to impose $\Phi_{1,6-9} \approx 0$ when a weakly magnetized liquid and a coil are considered. For very large simulation domains the more practical magnetic insulation condition $\Phi_{1,6-9} = \Psi_{1,6-9} = 0$ may be imposed.

3.3.1. $\Phi - \Psi$ uncoupling and virtual magnet substitution

From the structure of Eqs. (17) and (20) and the magnetic boundary conditions in Eqs. (25a) and (26a), the uncoupling between Ψ and Φ becomes evident. Both fields are computed separately, and Ψ does not depend on the deformation of the ferrofluid volume in the domain A. In other words, Ψ could be calculated at the beginning of the simulation and then implemented as an invariant source term in substitution of Eq. (13b). This is advantageous from the computational perspective, as the number of variables of the system is reduced and specific domains or subdomains are no longer needed. The only purpose of the boundary domains B-E would then be to ensure the convergence of Φ to the true solution by imposing the dipole approximation given by Eq. (26b) sufficiently far away from the ferrofluid. However, this approach also limits the scope and flexibility of the simulation framework, particularly for 3D problems without analytical solutions for Ψ. For this reason, both magnetic potentials are solved numerically in this work.

Although Eq. (25a) provides an exact boundary condition for any axisymmetric current distribution, the Φ field induced by magnetized media has to converge to the dipole approximation given by Eq. (26a). Consequently, if $\mathrm{E_c}$ is occupied by a magnet, larger simulation domains are required to guarantee convergence. It would be desirable, from a computational perspective, to have an exact boundary condition also in that case, limiting the dipole approximation to the magnetized region A. To overcome this issue, it should be noted that the $\boldsymbol{B}_m$ flux produced by a magnet can be described by two equivalent magnetic virtual currents: (i) a volume term $\boldsymbol{J}_m = \nabla\times\boldsymbol{M}_m$ distributed in the magnet volume, where $\boldsymbol{M}_m$ is the magnetization field, and (ii) a surface term $\boldsymbol{K}_m = \boldsymbol{n}\times[\boldsymbol{M}_m]$, with $\boldsymbol{n}$ denoting the normal to the interface and $[\boldsymbol{M}_m]$ the magnetization jump across it.

For a vertically magnetized cylindrical magnet with uniform magnetization $\boldsymbol{M}_m = M_m\boldsymbol{e}_z$, the equivalence results in a system of electrical currents with a volume density term $\boldsymbol{J}_e = \boldsymbol{0}$ in $\mathrm{E_c}$ and a surface density term $\boldsymbol{K}_e = M_m\boldsymbol{e}_\phi$ at the lateral wall. If the magnet has a height h, the equivalent electrical system can be modeled as a homogeneous distribution of $N_j\to\infty$ circular loops in the lateral wall with current M_mh/N_j. The magnetic field induced by this equivalent system is $\boldsymbol{H}_e = (\boldsymbol{B}_e/\mu_0)$, with $\boldsymbol{B}_e$ being the magnetic flux produced by the circular loops, which is identical to $\boldsymbol{B}_m$. Because the magnet induces a field $\boldsymbol{H}_m = (\boldsymbol{B}_m/\mu_0) - \boldsymbol{M}_m$ inside the magnetized volume, and $\boldsymbol{H}_m = (\boldsymbol{B}_m/\mu_0)$ outside, $\boldsymbol{H}_e$ is identical to $\boldsymbol{H}_m$ outside $\mathrm{E_c}$. In other words, the virtual magnet substitution procedure provides an exact analytical solution outside the magnet volume, leading to important computational advantages and faster model development.

3.4. Discretization of the simulation domain

The numerical procedure used in this study is a variation of the interface-tracking method developed by Herrada and Montanero for multiphase flows [38]. As shown in Fig. 2, the simulation domain is divided into five blocks that implement different discretization methods.

The blocks A, B, C, and D are mapped onto the square computational domains A: $[0\le s\le 1]\times[0\le\eta_A\le 1]$, B: $[0\le s\le 1]\times[0\le\eta_B\le 1]$, C: $[0\le s\le 1]\times[0\le\eta_C\le 1]$ and D: $[0\le s\le 1]\times[0\le\eta_D\le 1]$ by means of the analytical mappings

$$r_A = F(s,t),\quad z_A = G(s,t)\eta_A, \tag{27a}$$

$$r_B = F(s,t),\quad z_B = G(s,t) + [h_{BC} - G(s,t)]\eta_B, \tag{27b}$$

$$r_C = F(s,t),\quad z_C = h_{BC} + (h_{\mathrm{top}} - h_{BC})\eta_C, \tag{27c}$$

$$r_D = F(s,t),\quad z_D = h_{\mathrm{bot}}(1-\eta_D), \tag{27d}$$

where $h_{\mathrm{top}} = 0.15$ m ($h_{\mathrm{bot}} = -0.1$ m) denotes the top (bottom) height of the domain, and $h_B = 0.1$ m defines the transition height between B and C.

The domain E is built following the same approach, but in addition to concentrating points next to the domains A-D and adapting to their deformation, this block also has the functionality of defining the subdomain $\mathrm{E_c}$ and concentrating points close to its boundaries. In an early version of this work, these requirements were addressed by means of a meshfree discretization of domains D and E. However, that approach resulted in the ill-conditioning of the nodes that interfaced with blocks A-C, an excessive numerical error, and reduced tolerance to fluid deformation [66]. In the present framework, instead, nonsingular transformations of the form

$$r_E = F_E(s_E), \quad z_E = G_E(s_E, \eta_E, t), \tag{28}$$

mapped onto the square computational domain $[0 \le s_E \le 1] \times [0 \le \eta_E \le 1]$ are implemented in E. The radial and vertical position of the points are fixed with the exception of the subdomain between A-D and E$_c$, which follows the quasi-elliptical mapping [67]

$$F_E = F_E^*, \tag{29a}$$

$$g_{22}\frac{\partial^2 G_E}{\partial s_E^2} + g_{11}\frac{\partial^2 G_E}{\partial \eta_E^2} - 2g_{12}\frac{\partial^2 G_E}{\partial s_E \partial \eta_E} = 0, \tag{29b}$$

with boundary conditions

$$8\prime: \ \frac{\partial G_E}{\partial s} = 0, \tag{30a}$$

$$10-13: \ G_E = G_{A-D}, \tag{30b}$$

$$7: \ G_E = h_{\text{top}}, \tag{30c}$$

$$9: \ G_E = h_{\text{bot}}, \tag{30d}$$

where 8’ denotes the line parallel to 8 that touches the left wall of E$_c$, F_E^* is an imposed radial distribution, and the coefficients take the form

$$g_{11} = \left(\frac{\partial G_E}{\partial s_E}\right)^2 + \left(\frac{\partial F_E}{\partial s_E}\right)^2, \tag{31a}$$

$$g_{22} = \left(\frac{\partial G_E}{\partial \eta_E}\right)^2 + \left(\frac{\partial F_E}{\partial \eta_E}\right)^2, \tag{31b}$$

$$g_{12} = \frac{\partial G_E}{\partial \eta_E}\frac{\partial G_E}{\partial s_E} + \frac{\partial F_E}{\partial \eta_E}\frac{\partial F_E}{\partial s_E}. \tag{31c}$$

Because the boundaries with A-D and the rest of E are fixed, this subdomain adopts the role of a sliding mesh, ensuring the connectivity between the magnetic source and the liquid and proper adaptation to fluid deformation.

All the derivatives appearing in the governing equations are expressed in terms of s, η, and t. Then, the resulting equations are discretized in the s direction using fourth-order finite differences with n_s and n_{s_E} stretched points. In the η direction, fourth-order finite differences are also employed with n_{η_A}, n_{η_B}, n_{η_C}, n_{η_D}, and n_{η_E} stretched points. This discretization strategy gives rise to meshes that automatically adapt to any variation of the free liquid interface. The results presented in this work are obtained using $n_s = 101$, $n_{s_E} = 99$, $n_{\eta_A} = 101$, $n_{\eta_B} = 41$, $n_{\eta_C} = 21$, $n_{\eta_D} = 61$, and $n_{\eta_E} = 221$. The employment of fourth-order finite differences over a second-order approach leads to lower truncation errors with marginal implementation efforts and a reasonable computational penalty. Most importantly, it allows reducing the number of points in the simulation domain. Further details on the finite differences implementation can be found in the Appendix B.

To compute the steady-state solution, all the equations of the system are solved together in a monolithic scheme with a Newton-Raphson approach. Second-order backward differences are used to compute the time derivatives (see Appendix B), and since the method is fully implicit, the time step is chosen to be sufficiently large to ensure that a steady state is reached in a single iteration. This value is set to 100 s. If the time-dependent interface deformation is explored instead, a time step of 0.01 s is employed to guarantee convergence to the solution (see Section 4.5). One of the main characteristics of this procedure is that the elements of the Jacobian matrix are obtained by combining analytical functions and the collocation matrices of all subdomains. This allows taking advantage of the sparsity of the resulting matrix to reduce the computational time on each Newton-Raphson iteration, which converges when the norm of the state error vector $d\boldsymbol{x}$ is smaller than 10^{-3}. It should be noted that the norm of the solution is at least of order 1 [38], and hence the 10^{-3} threshold ensures convergence, as observed in the results. On the other hand, the Newton-Raphson method exhibits quadratic convergence rates close to the final solution, which speeds up the computation

As a reference, the computation of a single Newton-Raphson iteration using an Intel Core i7-7820HQ CPU at 2.90 GHz with 32 Gb RAM takes between 60 and 120 s with the base mesh employed in this work. A single time step usually takes between 3 and 15 iterations to converge. The non-magnetic interface tracking method on which this work is based has already been shown to overcome existing models in terms of computational efficiency in Ref. [38].

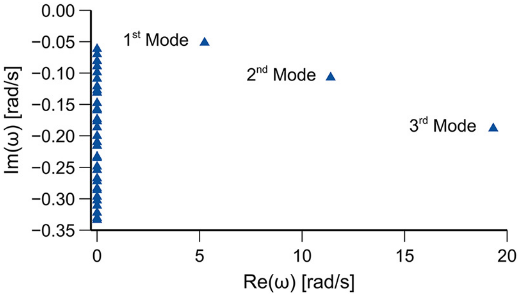

Fig. 3. Eigenfrequencies spectrum for $I = 10$ A. The first three dynamic modes are labeled.

3.5. Sloshing modes and free surface stability

The numerical procedure employed to compute the meniscus and time-dependent interface deformation is essentially the same that is used to determine the linear modes of the system [38]. The time derivatives are computed assuming that the time-dependent perturbation of any variable $\kappa(r, z, t)$ is of the form

$$\kappa(r, z, t) = \kappa_b(r, z, t) + \epsilon\delta\kappa(r, z, t)e^{-i\omega t} \quad (\epsilon \ll 1), \tag{32}$$

with $\kappa_b(r, z, t)$ denoting the steady-state solution, ϵ a small coefficient of perturbation, $\delta\kappa(r, z, t)$ the spatial dependence of the eigenmode for that variable, and $\omega = \mathrm{Re}(\omega) + i\mathrm{Im}(\omega)$ the eigenfrequency. The spatial dependence of the eigenmode is the solution of the generalized eigenvalue problem

$$\mathcal{J}_b^{(p,q)}\delta\kappa^{(q)} = i\omega \mathrm{Q}_b^{(p)}, \tag{33}$$

where $\mathcal{J}_b^{(p,q)}$ is the Jacobian of the system evaluated at the steady-state solution $\kappa_b^{(q)}$, and $\mathrm{Q}_b^{(p,q)}$ accounts for the time dependence of the problem (i.e. contains the time-dependent terms of the Jacobian). The resulting generalized eigenvalue problem is solved using the MATLAB EIGS routine. An example of the eigenfrequencies obtained with this method for $I = 10$ A is shown in Fig. 3. A *free-edge* condition with fixed contact angle is assumed in this process (i.e. the vertex A-B-E can move freely in the vertical direction, but keeping a constant θ_c). However, different implementations may consider a *stuck-edge* approach or more complex hysteresis mechanisms [22].

The dominant eigenmode is related to the largest growth factor $\mathrm{Im}(\omega)$. If such growth factor is negative, the damping ratio of the mode can be computed as $\zeta = -\mathrm{Im}(\omega)/|\omega|$, with $|\omega|$ being the norm of the eigenvalue. If $\mathrm{Im}(\omega)$ is positive, the meniscus becomes asymptotically unstable. This result is of particular importance for low-gravity magnetic liquid positioning applications, as it can be used to size the magnetic actuators of the system [68]. Further details on the computation of the eigenfrequencies and eigenmodes of the system can be found in Ref. [38].

4. Numerical results

4.1. Case of analysis

The ESA *Drop Your Thesis!* 2017 experiment *The Ferros* [41], that studied the axisymmetric oscillations of a ferrofluid solution in microgravity, is taken as a baseline for the analysis. The experiment is particularly well suited for the validation of the numerical framework introduced in this work because it (i) reports the first two axisymmetric modal frequencies of a continuous interface, (ii) exposes the ferrofluid to strong surface tension forces, and (iii) employs an inhomogeneous magnetic field. These three conditions conform the most general case of capillary ferrohydrodynamic flow and, to the best knowledge of the authors, are not present in any other published experiment.

The experimental setup, represented in Fig. 4, is composed of a mobile and a fixed structure. The former slides over the latter by means of two linear actuators, and holds two identical assemblies with equivalent experiments separated 368 mm. Each assembly includes a cylindrical vessel similar to the one represented in Fig. 1 that holds the liquid while a $N = 200$ turns copper coil with 94.25 mm mean radius imposes a static magnetic field. An axisymmetric free surface oscillation is first induced in microgravity by ZARM's drop tower catapult, that launches the experiment from the bottom of the facility, and then by a percussion mechanism that displaces the mobile structure vertically along the rails following a sinusoidal profile in the middle of the flight. The oscillations of the center of the fluid surface are recorded by a visualization system located on top of each container. The setup was launched five times at ZARM's drop tower in November 2017 with varying current intensities. The catapult mode produces 9.3 s of microgravity conditions with a maximum residual of 10^{-5} ms^{-2} Further details on ZARM's drop tower can be found in Ref. [69].

Both transparent liquid tanks have an inner diameter of 11 cm, a height of 20 cm, and are filled up to 5 cm with 475 ml of a 1:10 water solution of the commercial Ferrotec EMG-700 ferrofluid. The properties of the solution in the containers, that employ 10 nm particles, are reported in Table 1.

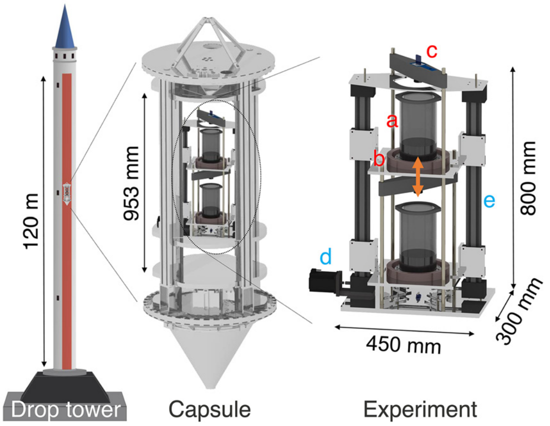

Fig. 4. From left to right, ZARM's drop tower, drop capsule, and setup of the ESA *Drop Your Thesis!* 2017 *The Ferros* experiment [41]. The setup has a mobile structure (red labels) with two identical assemblies that include (a) cylindrical ferrofluid containers, (b) magnetic coils, and (c) detection systems. The structure slides over a fixed frame (blue labels) with (d) a stepper engine actuator, and (e) two linear modules, as indicated by the orange arrow.

Table 1
Physical properties of the ferrofluid solution employed in the ESA *Drop Your Thesis!* 2017 experiment with their standard deviations [41].

Tank	ρ (g/ml)	μ (cP)	σ (mN/m)	θ_c(°)
Upper	1.012 ± 0.008	1.445 ± 0.005	62.39 ± 1.02	67 ± 6
Lower	1.020 ± 0.002	1.448 ± 0.007	61.7 ± 0.95	55 ± 4

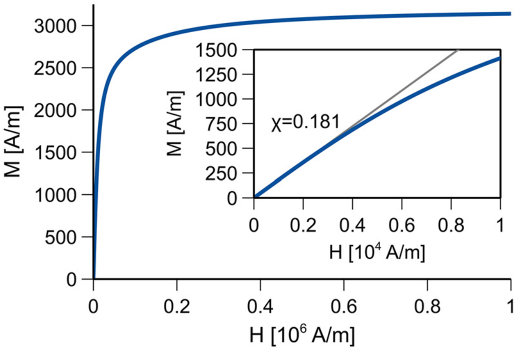

Fig. 5. Measured magnetization curve of the 1:10 vol EMG-700 ferrofluid solution.

The magnetic properties of the ferrofluid solutions were measured after the experimental campaign with a MicroSense EZ-9 Vibrating Sample Magnetometer. Figure 5 represents their magnetization curve, characterized by an initial susceptibility $\chi = 0.181$ and saturation magnetization $M_s = 3160 \pm 100$ Am^{-1}. The curve is fitted with Eq. (18), resulting in $a_M = 459.70$ Am^{-1}, $b_M = 2747.15$ Am^{-1}, $c_M = 5.73 \cdot 10^{-6}$ mA^{-1}, $d_M = 1.03 \cdot 10^{-4}$ mA^{-1}, and $e_M = 0$. Further technical details on the experimental setup and the ESA *Drop Your Thesis!* 2017 experiment *The Ferros* can be found in Refs. [40,41].

4.2. Verification

The ferrohydrodynamic simulation framework here introduced extends the capillary model presented in Ref. [38] by considering the magnetic interaction. After verifying that the fluid-dynamic results in the absence of magnetic fields are consistent with previous works, the verification and validation processes focus on the magnetic modules.

4.2.1. Field-free solution

The dynamic response predicted by the interface-tracking framework on which this work is based has already been validated with experiments on liquid bridges at the International Space Station [38]. For completeness, however, an extended verification is here presented for the axisymmetric liquid sloshing problem. The dimensionless variables

$$\mathrm{Bo} = \frac{\rho g R^2}{\sigma}, \quad \Omega_1^2 = \frac{\rho R^3 [\mathrm{Re}(\omega_1)]^2}{\sigma}, \quad \mathrm{Oh}^2 = \frac{\eta^2}{\rho \sigma R},$$

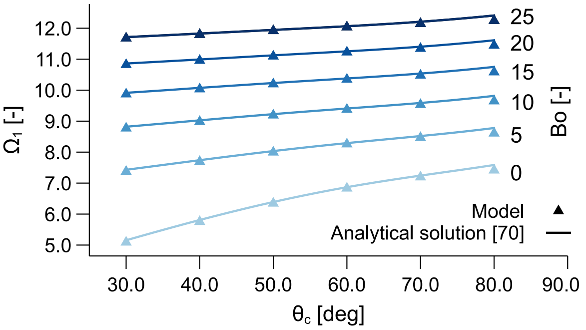

Fig. 6. Real fundamental axisymmetric frequency as a function of the contact angle and gravity level compared with analytical results from Yeh [70].

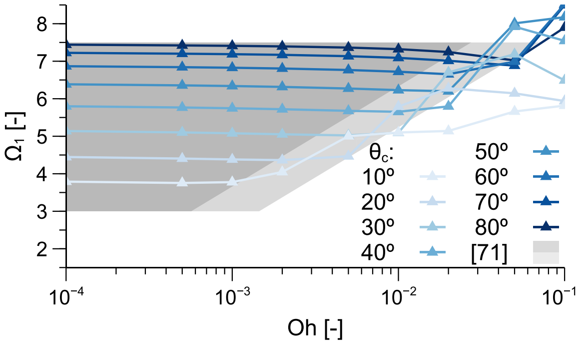

Fig. 7. Numerical results for the dimensionless frequency as a function of the Ohnesorge number and contact angle compared with envelope data from Gerstmann and Dreyer [71].

that correspond to the Bond number, the dimensionless real fundamental frequency, and the Ohnesorge number, respectively, are employed in the validation together with the previously defined damping ratio ζ in consistency with the original sources of data.

Figure 6 depicts the dimensionless real fundamental axisymmetric frequency of the tank described in Section 4.1 for a range of contact angles and Bond numbers. An inviscid liquid is employed to run the simulations, which are then compared with the analytical model developed by Yeh in Ref. [70]. The results are in perfect agreement and demonstrate that the implementation of the inviscid non-magnetic terms (in particular, surface tension) are appropriate.

Next, the modal response of the liquid is explored for different contact angles and Ohnesorge (viscosity) levels in Fig. 7 and compared with free-edge envelope computations from Gerstmann and Dreyer [71]. Following their discussion, gray patches define parametric spaces where surface oscillations are observable, which are bounded by analytical approximations for small Oh at $\theta_c = 0^\circ$ ($\Omega_1^{\min} = 3$), $\theta_c = 90^\circ$ ($\Omega_1^{\max} = 7.5$), and transition limits of the form $\Omega_1 = a + b\ln(\mathrm{Oh})$. The dark and light gray areas denote the viscous damping and boundary layer-dominated regimes, respectively. The second is characterized by the the enlargement of the boundary layer and the increase of the frequency with the Ohnesorge number caused by the reduction in the effective liquid radius. The interested reader is referred to Ref. [71] for a comprehensive discussion of these effects. In the context of this section, however, the main conclusion is that numerical results are in perfect agreement with the reference study, validating the implementation of viscous terms and no-slip boundary conditions at the walls of the tank.

The dependence of the damping ratio ζ with the Ohnesorge number and contact angle is finally reported in Fig. 8 and compared with the envelope computed by Gerstmann and Dreyer [71]. Again, the results are in perfect agreement and reproduce the transition from linear to non-linear regimes as Oh increases.

The previous results have been expressed in dimensionless variables for consistency with the sources of data. However, it is important to note that the ferrohydrodynamic model introduced in this work is dimensional. There is an inherent benefit in using dimensionless variables in low-gravity fluid mechanics (and, in general, capillary) problems, but this practice is far less beneficial in the ferrohydrodynamic framework due to the dependence of the solution on the magnitude, direction, and distribution of the inhomogeneous magnetic force. An excellent review of analytical low-gravity fluid mechanics methods is given by Myshkis and coworkers in Ref. [47].

4.2.2. Magnetic model

The magnetic field $\boldsymbol{H}$ is first compared in Fig. 9 with a finite elements Comsol Multiphysics magnetic model. The model takes the equilibrium ferrofluid interface and, assuming the same materials, computes the magnetic field without solving

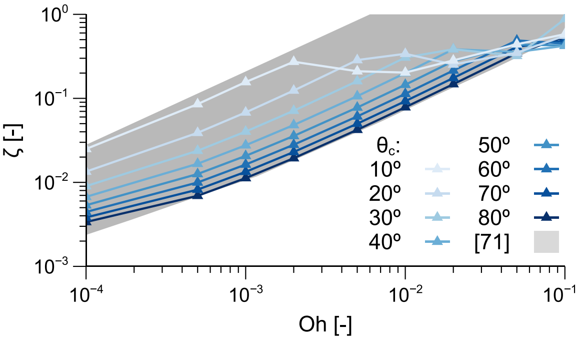

Fig. 8. Numerical results for the damping ratio as a function of the Ohnesorge number and contact angle compared with envelope data from Gerstmann and Dreyer [71].

the Navier-Stokes equations. Further details on its implementation can be found in the Appendix C. Both solutions are in excellent agreement, reflecting the appropriate implementation of Eqs. (10) and (11) and their axisymmetric formulations in Section 3.2. Similar levels of agreements are observed when the coil is substituted by a vertically magnetized magnet but, as described in Section 3.3.1, larger simulation domains are needed.

Figure 10 compares the magnetic force density for $I = 20$ A with the control model in Comsol Multiphysics. The distributions are virtually identical, which verifies the implementation of the magnetic force in Eq. (6c). The force depends on the spatial derivatives of the magnetic field is then highly sensitive to irregularities in $\boldsymbol{H}$ and $\boldsymbol{M}$. In the figure, however, such irregularities are only observed in the finite elements Comsol Multiphysics model, reflecting the high stability of the fourth-order finite differences scheme employed in this work. The irregularities in the Comsol solution are just a consequence of the gradient computation step and do not reflect an underlying problem with the simulation. The implementation of the magnetic force term in the momentum balance is verified in Fig. 11. According to Eq. (9b), the steady state pressure lines must be coincident with the constant H^2 lines for a linearly magnetized liquid. After implementing a constant magnetic

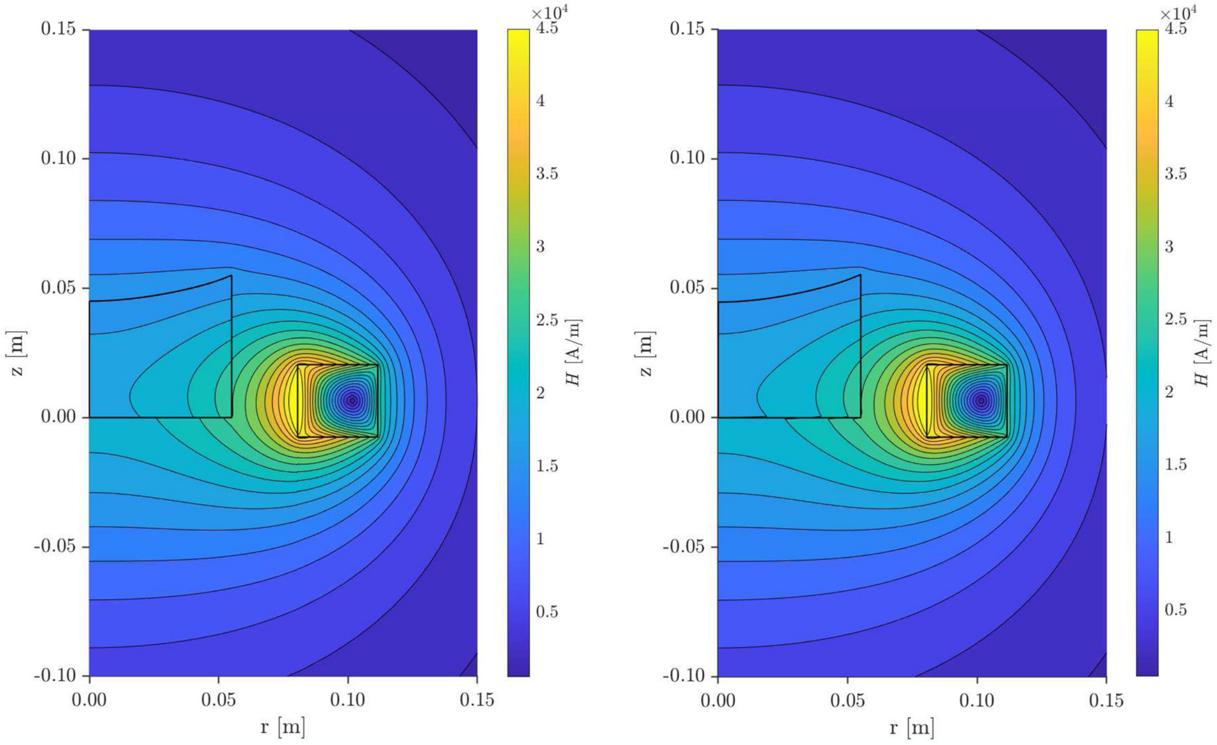

(a) Coupled FHD model (b) Comsol Multiphysics

Fig. 9. Magnetic field comparison for $I = 20$ A.

Table 2
Intermediate results for representative positions in domain A as a function of the applied current intensity.

I [A]	r [cm]	z [cm]	ϕ [A]	ψ [A·m]	H [A/m]	F_m [N/m^3]	p^* [Pa]	η [mPa·s]
10	1	1	0.52	-13.38	9612.92	32.77	1.80	1.447
	5	1	14.50	-7.64	12481.52	331.13	7.20	1.448
	5	5	9.81	11.64	8036.53	193.77	-0.78	1.446
15	1	1	0.78	-17.11	14630.95	63.03	4.69	1.448
	5	1	21.76	-9.64	18907.84	593.66	14.64	1.449
	5	5	14.72	14.68	12076.60	385.32	-0.66	1.448
20	1	1	1.04	-19.58	19725.66	96.22	8.09	1.449
	5	1	29.01	-10.93	25390.19	865.30	22.81	1.450
	5	5	19.62	16.69	16135.73	605.11	-0.51	1.449

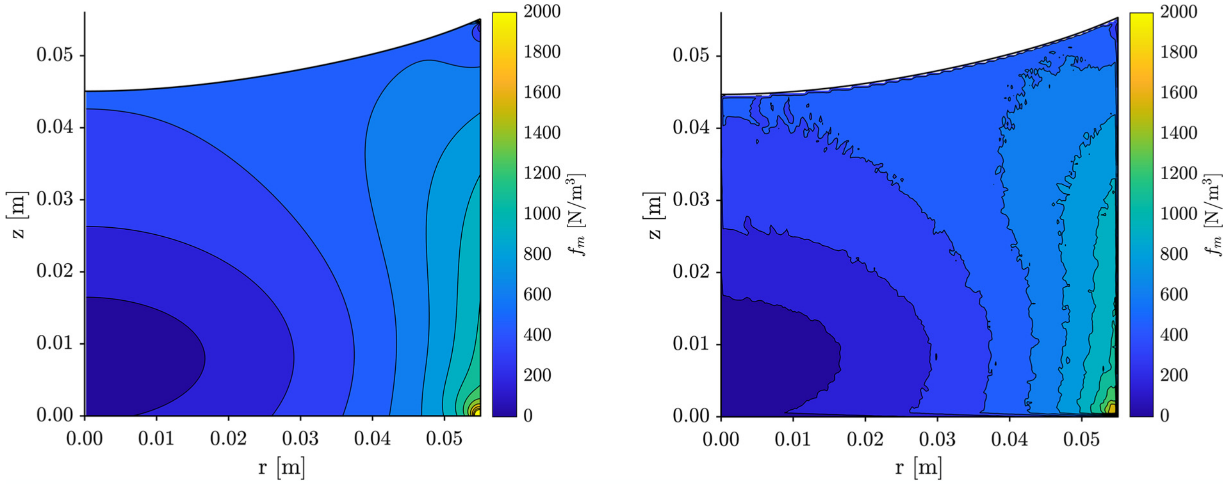

(a) Coupled FHD model

(b) Comsol Multiphysics

Fig. 10. Force density module comparison for $I = 20$ A.

susceptibility $\chi^{\mathrm{vol}} = 0.1$, the comparison between both plots reflects the expected behavior. Here and in the rest of the manuscript, the pressure is referred to the value at the B side of line 15.

Finally, quantitative intermediate results are reported in Table 2 for different locations inside domain A as a function of the applied current intensity. The reader may find this useful as a reference for future works.

4.2.3. Equilibrium and virtual magnet substitution

The previous section verifies that (i) the magnetic model produces the desired magnetic field, (ii) such field results in the appropriate magnetic force, and (iii) the magnetic force is properly implemented in the system. The next logical step consists on comparing the equilibrium solution with previous models

In the magnetic sloshing problem, the equilibrium free surface profile - or *meniscus* - defines the steady-state solution of the system. Such profile experiences very small deformations in the ESA *Drop Your Thesis!* 2017 - *The Ferros* experiment, making it unsuitable for comparison, and so a different setup is chosen. The model and case of analysis introduced in Ref. [22] are analyzed employing the virtual magnet substitution approach introduced in Section 3.3.1. A 5 cm radius cylindrical tank filled up to 5 cm with the ferrofluid described in Section 4.1 is exposed to the magnetic field produced by a 28 mm radius, 3 mm height disc magnet with a 5 mm hole in its center. This magnet is located 1 mm below the bottom of the container, and is magnetized at $M_m = 1500$ kAm^{-1} along the z-direction. The resulting $\boldsymbol{B}$ field corresponds to the one produced by an internal virtual surface current $\boldsymbol{K}_{e,i} = -M_m \boldsymbol{e}_\phi$ at $r = 2.5$ mm, and an external virtual surface current $\boldsymbol{K}_{e,e} = M_m \boldsymbol{e}_\phi$ at $r = 28$ mm. 20 equispaced circular loops with currents of 375 A are employed on each side to compute the Ψ potential of this equivalent system.

Although the assimilation of virtual magnetization currents as electric currents cannot be adopted in the computation of the magnetic field $\boldsymbol{H}$ inside the magnet, an exact solution is still obtained in the external domain. Indeed, the magnetic field represented in Fig. 12(a), obtained with the virtual magnet substitution procedure, is in excellent agreement with the previous quasi-analytical magnetic sloshing model [22] shown in Fig. 12(b). In the second case, the magnetic problem is solved by iterating with the Comsol Multiphysics magnetic model described in the Appendix C. Both solutions show a characteristic protuberance at the center of the meniscus, which results from the tendency of the liquid to follow the constant Bo_{mag} (or $\boldsymbol{H}$) lines when surface tension is weakest. Previous works have predicted and reported this behavior [22,72].

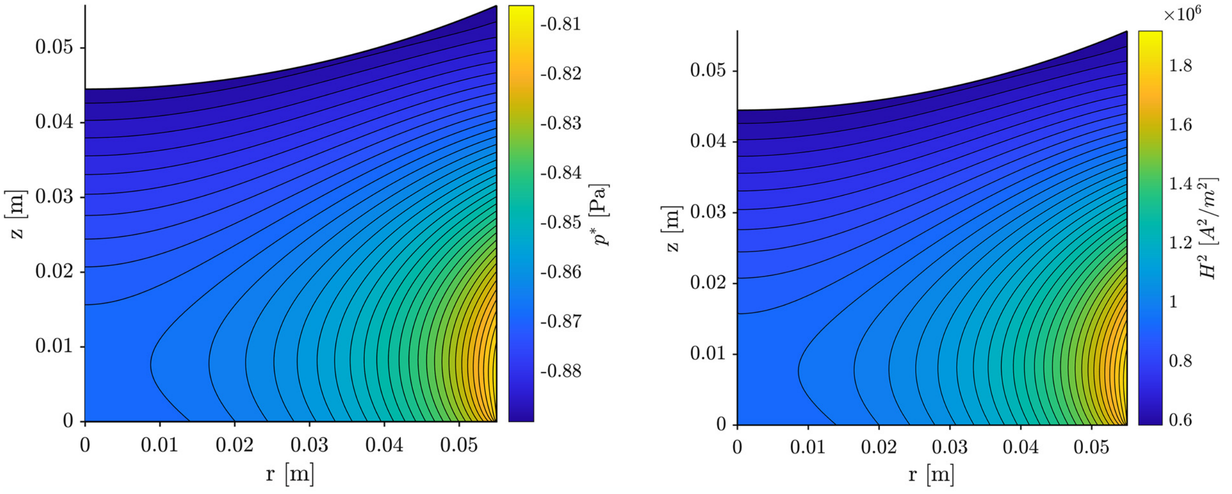

(a) Pressure

(b) Magnetic field

Fig. 11. Comparison of presssure and magnetic field lines for a paramagnetic fluid with $\chi^{\text{vol}} = 0.1$ at $I = 1$ A.

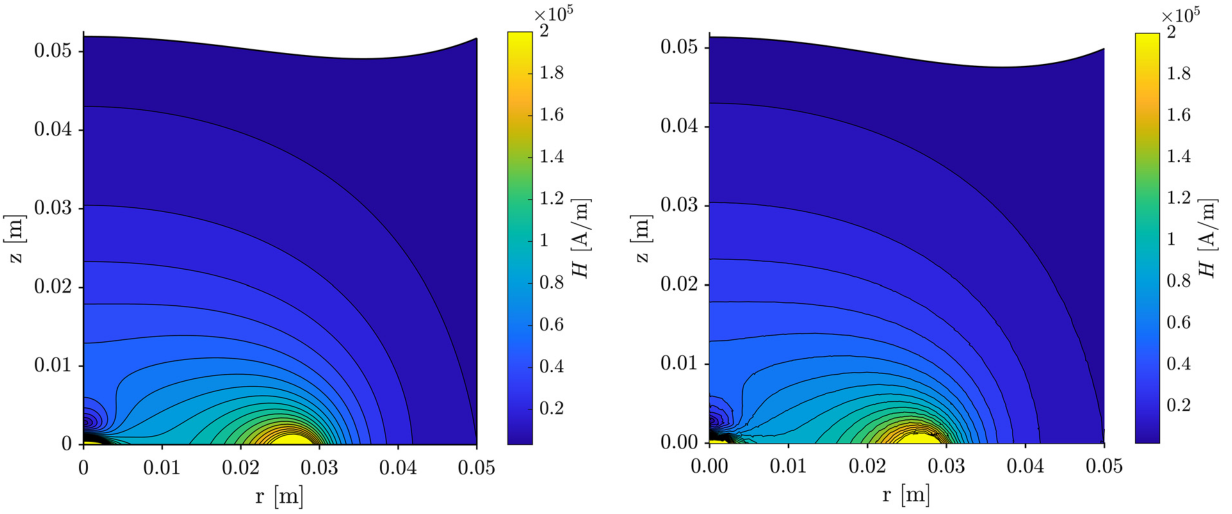

(a) Coupled FHD model

(b) Quasi-analytical model [22]

Fig. 12. Comparison of magnetic fields and meniscus produced by a 3 mm height, 27.5 mm external radius magnet with a central 5 mm radius hole located 1 mm below the container. The virtual magnet substitution method described in Section 3.3.1 is employed.

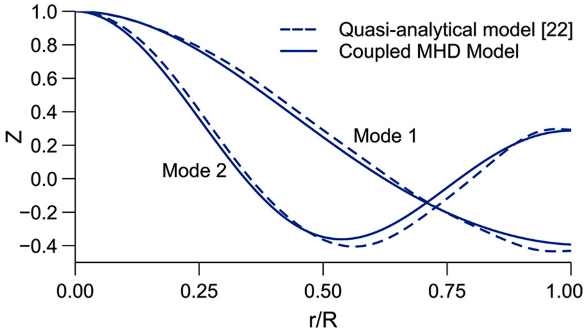

Fig. 13. Comparison of first two fundamental modes for $I = 20$ A.

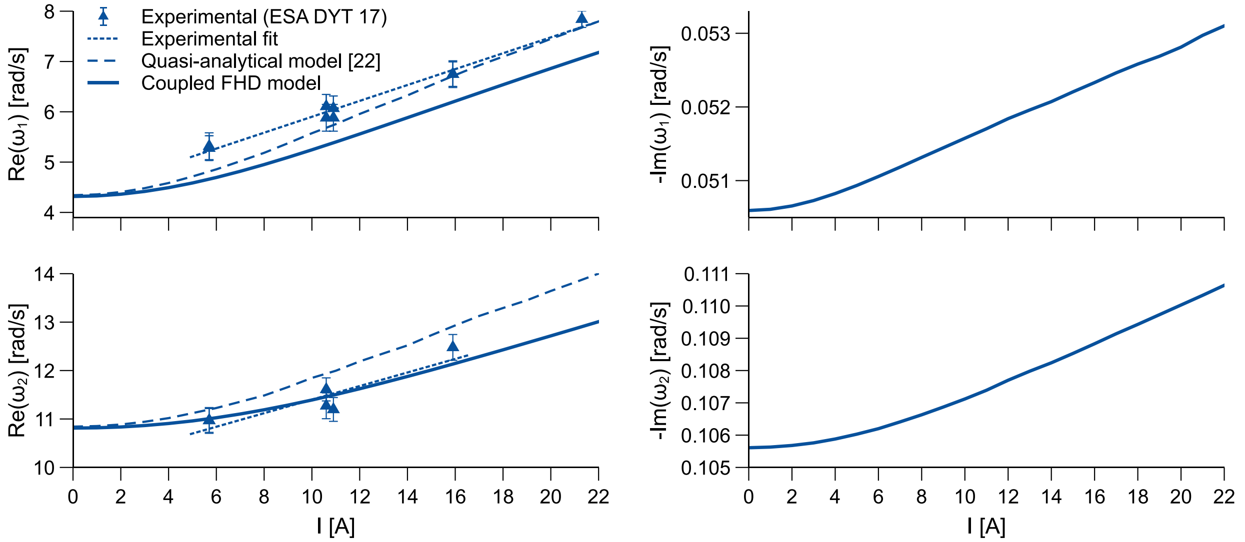

(a) Upper container

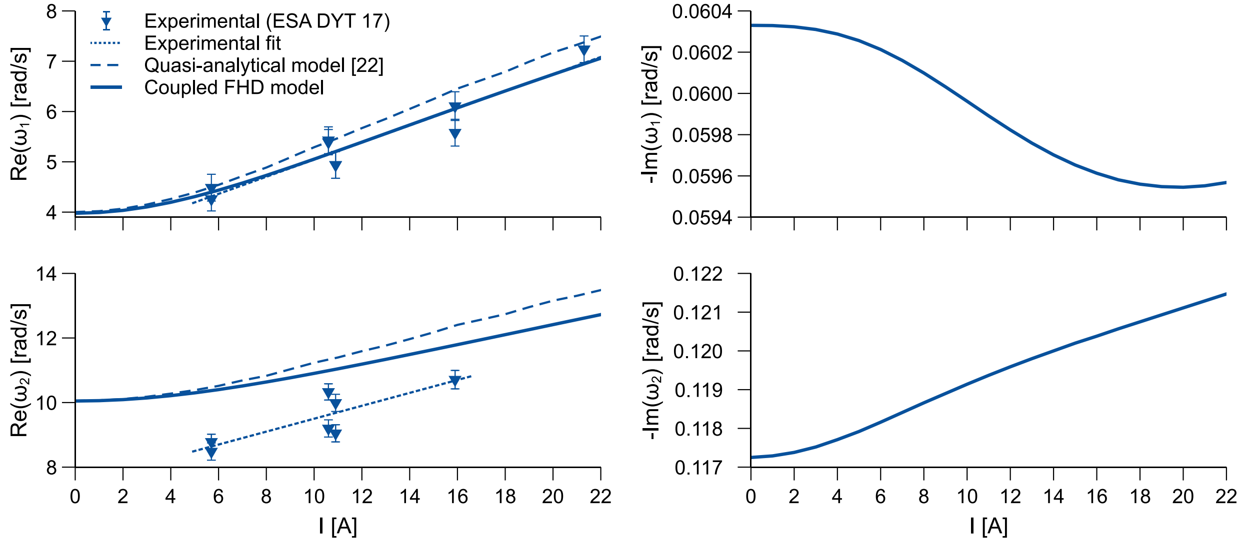

(b) Lower container

Fig. 14. First two axisymmetric natural sloshing frequencies compared with a previous quasi-analytical model [22] and experimental measurements obtained during the ESA *Drop Your Thesis!* 2017 campaign [41].

4.2.4. Modal shapes

Figure 13 compares the shape of the first two axisymmetric modes obtained using the procedure described in Section 3.5 with predictions from the quasi-analytical model in Ref. [22] for $I = 20$ A. The plot shows the normalized modal vertical displacement Z of the surface as a function of the non-dimensional radius r/R. An excellent overall agreement is observed, but small disagreements are produced due to the inherent differences between both methods. While the procedure here presented is based on the numerical solution of an eigenvalue problem, the quasi-analytical solution relies on a set of suitable primitives and admissible functions that are employed in Ritz's method.

4.3. Dynamic response

As discussed in Section 4.1, the geometry and physical properties of the ESA *Drop Your Thesis!* 2017 experiment *The Ferros* [41] are subsequently adopted in the validation of the dynamic response of the model. Among the potential validation metrics, the natural free surface oscillation frequencies arise as the easiest to measure and the most relevant for the development of mechanical analogies [46]. Furthermore, they condense the effect of the magnetic settling force in the fluid system.

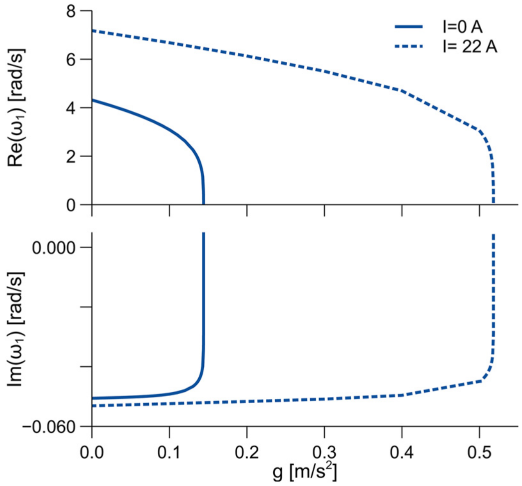

Fig. 15. Fundamental axisymmetric frequency as a function of the applied destabilizing inertial acceleration for magnetic ($I = 22$ A) and non-magnetic ($I = 0$ A) cases.

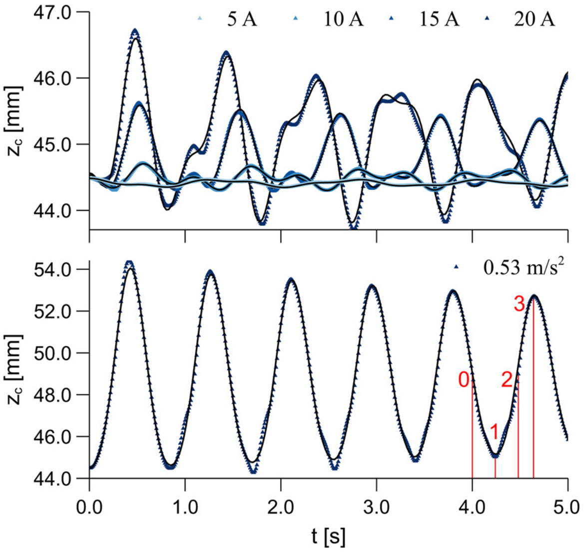

Fig. 16. Time evolution of the center of the free surface after the application of magnetic (top) and inertial (bottom) step loads in microgravity. The modal fits reported in Eq. (34) and Table 5 are superposed.

The first two axisymmetric free surface oscillation frequencies are reported in Fig. 14 for the upper and lower containers of the setup depicted in Fig. 4 as a function of the coils current intensity. Predictions from the numerical framework are compared with results from a previous quasi-analytical inviscid magnetic surface oscillations model [22] and with experimental data [41]. The experimental setup has a second coil that is not modeled in the simulation domain (see Figs. 2 and 4), but since its contribution increases the fundamental oscillation frequency in just a 0.45%, it is considered negligible. Two comparison metrics can be extracted from Fig. 14: the vertical shift between curves, and their slope. The former is attributed in Ref. [41] to the accumulation of errors in the non-magnetic parameters of the system. This conclusion is backed up by (i) the large uncertainties reported in Table 1 for contact angles and surface tension coefficients, (ii) the strong dependence of the natural oscillation frequencies on such parameters, explored in Fig. 6, (iii) the linearity of the current-frequency curve, and (iv) the field-independent experimental shift of $\sim 0.9\sim 0.9$ rads^{-1} between the fundamental frequencies of upper and lower containers. This constant shift points to the field-free frequency upon which the magnetic response is built, and hence to the non-magnetic parameters that determine it. It also shows that such initial uncertainty has little or no effect on the frequency-current response of the system because both lines are practically parallel, as quantified in the next paragraph. This is further supported by the fact that the magnetic force is too weak to produce significant deformations on the interface, and thus any potential surface tension or contact angle discrepancy will be unable to alter the magnetic response if the meniscus geometry is kept essentially frozen.

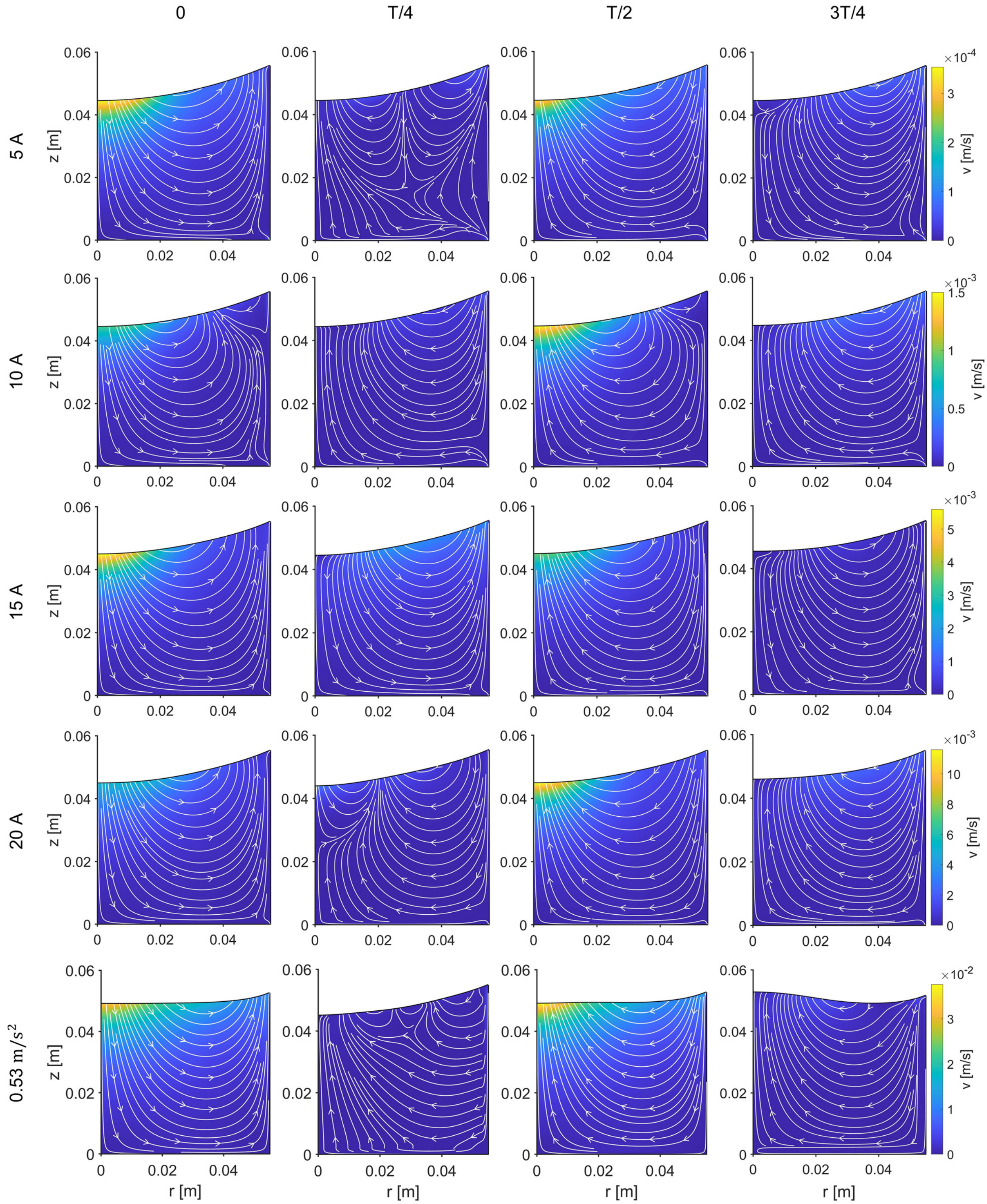

Fig. 17. Streamlines after the application of magnetic (5–20 A) and inertial (0.53 ms^{-2}) step loads in microgravity. Successive time points reflect the first node (0), minimum ($T/4$), second node ($T/2$), and maximum ($3T/4$) of the displacement of the center of the surface, as indicated in Fig. 16.

Table 3
Complex fundamental axisymmetric frequencies as a function of mesh density in region A ($n_s \times n_{\eta_A}$) for different current intensities.

	Re(ω_1) [rad/s]			Im(ω_1) [rad/s]		
	91 × 91	101 × 101	111 × 111	91 × 91	101 × 101	111 × 111
0 A	4.3179 (+0.0269%)	**4.3168**	4.3159 (-0.0216%)	-0.0506 (+0.0046%)	**-0.0506**	-0.0507 (+0.1878%)
5 A	4.5862 (+0.0243%)	**4.5851**	4.5842 (-0.0191%)	-0.0510 (+0.1241%)	**-0.0509**	-0.0510 (+0.1013%)
10 A	5.2454 (+0.0210%)	**5.2443**	5.2435 (-0.0157%)	-0.0518 (+0.4098%)	**-0.0516**	-0.0515 (-0.1069%)
15 A	6.0486 (+0.0197%)	**6.0474**	6.0466 (-0.0139%)	-0.0526 (+0.7670%)	**-0.0522**	-0.0520 (-0.3681%)
20 A	6.8627 (+0.0193%)	**6.8614**	6.8605 (-0.0132%)	-0.0534 (+1.1809%)	**-0.0528**	-0.0525 (-0.5821%)

Table 4
Complex second axisymmetric frequencies as a function of mesh density in region A ($n_s \times n_{\eta_A}$) for different current intensities.

	Re(ω_2) [rad/s]			Im(ω_2) [rad/s]		
	91 × 91	101 × 101	111 × 111	91 × 91	101 × 101	111 × 111
0 A	10.8173 (+0.0518%)	**10.8117**	10.8074 (-0.0403%)	-0.1078 (+2.0552%)	**-0.1056**	-0.1043 (-1.2539%)
5 A	10.9659 (+0.0509%)	**10.9603**	10.9560 (-0.0395%)	-0.1083 (+2.1204%)	**-0.1060**	-0.1046 (-1.3018%)
10 A	11.3980 (+0.0499%)	**11.3924**	11.3880 (-0.0383%)	-0.1096 (+2.3165%)	**-0.1071**	-0.1056 (-1.4433%)
15 A	12.0173 (+0.0498%)	**12.0113**	12.0068 (-0.0376%)	-0.1114 (+2.6019%)	**-0.1085**	-0.1067 (-1.6841%)
20 A	12.7226 (+0.0506%)	**12.7162**	12.7115 (-0.0374%)	-0.1132 (+2.9240%)	**-0.1100**	-0.1079 (-1.8967%)

Unlike the vertical frequency shift, the frequency-current slopes reflect the magnetic response of the system. The experimental slope of the fundamental frequency at the upper container is 0.158 rads^{-1}A^{-1} with [0.138,0.178] rads^{-1}A^{-1} 95% confidence interval (CI), while in the lower vessel it results in 0.170 rads^{-1}A^{-1} with [0.121,0.219] rads^{-1}A^{-1} 95% CI. These CIs do not include the 0.187 rads^{-1}A^{-1} slope of the analytical model at the upper vessel, but include the 0.186 rads^{-1}A^{-1} value of the lower tank. On the contrary, the numerical model presented in this work matches almost perfectly the experimental slopes, with 0.161 rads^{-1}A^{-1} for the upper container and 0.167 rads^{-1}A^{-1} for the lower. As expected from the field-free analysis presented in Fig. 6, the non-magnetic solution ($I = 0$ A) is also in excellent agreement with the quasi-analytical model.

The second fundamental axisymmetric modes are also reported in Fig. 14 for those cases where they are observable. The amplitude of the second mode is much smaller than the first, and so harder to detect. Because in some experiments the second mode could not be recovered, the number of data points is significantly smaller. In addition, its higher oscillation frequency and complex shape makes it more sensitive to disturbances in the contact line. This explains the horizontal bias in the plots and why the experimental slopes of 0.136 rads^{-1}A^{-1} with [0.049, 0.222] rads^{-1}A^{-1} 95% CI (upper container) and 0.202 rads^{-1}A^{-1} with [0.054, 0.349] rads^{-1}A^{-1} 95% CI (lower container) have such wide CIs. As pointed out in Ref. [41], this large uncertainty effectively renders any comparison with the theoretical slopes statistically meaningless. Still, results are given for completeness.

The differences between inviscid quasi-analytical [22] and numerical results cannot be explained by the effects of liquid viscosity, that accounts for just a 0.6% reduction of the real frequency component. The remaining discrepancy may be attributed to the differences in modal shapes shown in Fig. 13, but there is a deeper reason that could cause it. While Ref. [22] applies a first-order perturbation to an equilibrium solution while considering a constant magnetic environment, the monolithic numerical framework here introduced linearizes the full fluid-magnetic solution around the equilibrium state. Therefore, the magnetic terms are also linearized and contribute to the modal response. If any, this is an important reason for choosing monolithic approaches over partitioned schemes when studying coupled ferrohydrodynamic problems.

Recent works have also observed the increase in the imaginary component (damping) with the applied magnetic field [44]. However, the damping ratios measured in Ref. [41] for the ESA *Drop Your Thesis!* 2017 campaign are one order of magnitude larger than in Fig. 14. The same damping bias is observed at the UNOOSA DropTES 2019 StELIUM experiment [44]. Because the viscosity of the ferrofluid employed in both experiments was measured with a rheometer under zero-field conditions, the reader may be tempted to attribute this effect to the magnetic interaction. Magnetic nanoparticles, like any magnetic dipole, tend to align with the magnetic field. Although the reorientation is assumed instantaneous in this work, this may not be true for ferrofluids with high vortex viscosity or subject to high-frequency alternating magnetic fields. Such liquids exhibit an apparent increase in the shear viscosity coefficient η [64]. However, the application of Shliomis' shear model [73] to the problem under study results in a viscosity variation of just ~1% at 10^6 Am^{-1}, justifying the adoption of the symmetrical constitutive relation in Eq. (4). The larger experimental damping may instead be caused by interfacial effects induced by the surfactant. Similar disagreements have been reported in previous experiments with water and hexadecane in Refs. [74] and [75], suggesting a large susceptibility of the effective viscosity of low viscosity liquids to surface contamination.

Real and imaginary frequency components are reported in Tables 3 and 4 for different current intensities and block A mesh densities. It should be noted that the configuration of block A determines the density of the rest of the simulation do-

Table 5
Fitting parameters defined in Eq. (34) for the time evolution of the center of the free surface reported in Fig. 16 for different step loads.

Step load	a_1 [m]	$\text{Im}(\overline{\omega}_1)$ [rad/s]	$\text{Re}(\overline{\omega}_1)$ [rad/s]	b_1 [-]	a_2 [m]	$\text{Im}(\overline{\omega}_2)$ [rad/s]	$\text{Re}(\overline{\omega}_2)$ [rad/s]	b_2 [-]	k_0 [m]
5 A	$5.158{\cdot}10^{-5}$	-0.0532	4.576	-0.0035	$2.2645{\cdot}10^{-5}$	-0.1180	10.916	-0.0634	0.0444
10 A	$-1.1093{\cdot}10^{-3}$	-0.0567	5.233	-0.0181	$1.2449{\cdot}10^{-4}$	-0.1073	11.345	-0.0611	0.0445
15 A	$-5.462{\cdot}10^{-4}$	-0.0515	6.045	-0.0334	$3.2057{\cdot}10^{-4}$	-0.1213	11.988	-0.0928	0.0448
20 A	$-1.063{\cdot}10^{-3}$	-0.0543	6.843	-0.0135	$-0.5423{\cdot}10^{-3}$	-0.1469	12.640	-0.0252	0.0451
0.53 ms^{-2}	$-4.866{\cdot}10^{-3}$	-0.0553	7.428	-0.0466	$-0.6506{\cdot}10^{-3}$	-0.1624	14.952	-0.1785	0.0487

main. The convergence of the base mesh (101×101 nodes) is demonstrated for real and imaginary components with errors below 0.05% and 1.9%, respectively. Furthermore, the error decreases with increasing densities, showing that the solution is mesh-independent. The imaginary terms are more sensitive to the mesh density, as they depend on the discretization of the boundary layer at the walls of the container. This motivates, in first instance, the adoption of the non-uniform nodal distribution in block A shown in Fig. 2.

4.4. Global stability

Understanding the stability properties of capillary interfaces is essential for numerous physical systems, from liquid bridges [75,76] to conduit geometries [77,78]. The classical literature, motivated by the development of propellant management devices for space applications, has devoted significant attention to this problem since the 1960s [46,47]. In low-gravity sloshing the stability is closely related to the concept of *critical load*, defined as the inertial acceleration that destabilizes a given interface. This is an important parameter for the design of propellant tanks [79]. Although the stability problem has been comprehensively studied since the Apollo era, its magnetic equivalent remains practically unexplored [68].

Figure 15 depicts the evolution of the fundamental axisymmetric frequency of the ESA *Drop Your Thesis!* 2017 problem as a function of the inertial acceleration g along the axis of the container. The transition to an unstable equilibrium regime is characterized by the sudden change of sign and the drop to zero of the imaginary and real components, respectively. While the non-magnetic interface breaks for a critical load of 0.1441 ms^{-2}, a value that is in agreement with analytical results from Myshkis and coworkers [47], the magnetic force stabilizes the system and pushes the limit up to 0.518 ms^{-2}. This represent a 359.5% critical load increase, and exemplifies how magnetic polarization forces may be employed to enhance the controllability of space propellants. Greater gains should be expected for systems employing high-density permanent magnets, like the magnetic sloshing control device proposed in Ref. [22].

4.5. Time-dependent analysis

To conclude the presentation of numerical results, Fig. 16 depicts the time-dependent vertical displacement z_c of the center of the free surface after the application of 5, 15, and 20 A step loads in microgravity. The response of the surface to a $\sim$ 0.53$\sim$0.53 ms^{-2} step acceleration in the absence of magnetic fields is shown for comparison. This value corresponds to the mean magnetic acceleration exerted by the coil on the interface at 20 A, which drives the dynamic response of the system according to the quasi-analytical model described in Refs. [22] and [45]. If the position of the center is fitted with a function of the form

$$z_c = \sum_{i=1}^{2} \left[a_i e^{\text{Im}(\overline{\omega}_i)t} \cos\left(\text{Re}(\overline{\omega}_i)t + b_i\right) \right] + k_0 \tag{34}$$

where a_i, b_i, $\overline{\omega}_i$, and k_0 are the fitting parameters for mode i, the results reported in Table 5 are obtained. It should be noted that $\overline{\omega}_i$ are estimations of the complex eigenfrequencies of the system. As expected, they match the real ($\text{Re}(\omega_i)$) and imaginary ($\text{Im}(\omega_i)$) magnetic frequency components computed in Table 3 and 4 with minimum errors. Those errors are caused by the inherent difficulties in observing the second eigenmode when superposed to other waves. This result verifies the implementation of the eigensolver described in Section 3.5 and the consistency of the solution.

As the magnetic step load increases in magnitude, so does the dynamic response of the interface. The 5 and 10 A excitations keep the wave amplitude below ~0.25 mm, but this value jumps to ~0.5 and ~1.5 mm for 15 and 20 A, respectively. It is important to note that the 0.53 ms^{-2} inertial load produces a wave that is three times larger than the 20 A counterpart that is supposed to resemble. The reason should be found in a slightly larger inertial load, reflected in its higher eigenfrequencies in Table 5, and the curved magnetic field contours at the interface shown in Fig. 9, that differ significantly from the horizontal equipotential lines of the inertial field. Since the horizontal equipotentials are further away from the field-free meniscus, once the excitation is applied the interface will acquire higher potential energies and produce larger amplitude oscillations.

Finally, Fig. 17 shows the streamlines associated with the cases covered in Fig. 16. Successive time points reflect the approximate first node (0), minimum ($T/4$), second node ($T/2$), and maximum ($3T/4$) of the displacement of the center of the surface. The four points chosen for the inertial wave are highlighted in Fig. 16. In the non-magnetic case, the same nodal flow patterns reported in Ref. [71] are observed. However, the magnetic cases also show an apparent boundary layer enlargement at the lower right corner of the container. This is presumably caused by the large localized magnetic forces induced by the coil and seems to be a feature of the magnetic sloshing problem. The minimum and maximum displacement points correspond to transition regimes and lead to more complex flow patterns with respect to the nodal cases. Higher order eigenmodes are clearly visible as counter rotational votexes in several plots (e.g. at $T/4$ for 5 A, 20 A, and the inertial case).

5. Conclusions

A fully coupled interface-tracking ferrohydrodynamic model has been developed to analyze the equilibrium, stability, modal response, and time-dependent evolution of magnetic liquids in axisymmetric surface tension-dominated multiphase flows using a highly efficient monolithic scheme. These characteristics enable the study of highly susceptible materials, such as ferrofluids, in a wide variety of ferrohydrodynamic problems.

Classical results and magnetic simulations in Comsol Multiphysics are employed to verify the field-free implementation of the model. The free surface oscillation frequencies are validated with experiments from the ESA *Drop Your Thesis!* 2017 *The Ferros* campaign, improving the estimations from a previous quasi-analytic approach [22]. The numerical framework is shown to determine the linear stability and nonlinear evolution of the interface, whose analysis hints at the existence of characteristic magnetically-induced flow patterns. From a technical perspective, these capabilities are essential for the design of novel magnetic propellant management devices in space [41].

Although the axisymmetric magnetic sloshing problem and the ESA *Drop Your Thesis!* 2017 configuration have been studied in this work, the numerical model finds application in additional scenarios interest. Those include the analysis of microfluidic systems involving highly susceptible magnetic liquids, liquid manipulation devices in space, or bubble/droplet growth, detachment, and displacement problems, among many others.

Declaration of Competing Interest

The authors declare no competing interests.

Data Availability

Data will be made available on request.

Acknowledgments

The project leading to these results has received funding from *la Caixa* Foundation (ID 100010434), under agreement LCF/BQ/AA18/11680099 and the Rafael del Pino Foundation Excellence Fellowship 2021. M.A.H. acknowledges the support of the *Ministerio de Economía y Competitividad* and *Junta de Andalucía* through Grants PID2019-108278RB-C31 and P18-FR-3623.

Appendix A. Magnetic force derivation

The magnetic stress tensor $\mathcal{T}_m$ has been widely used in classical an recent works to obtain the local distributions of magnetic forces on magnetically polarizable bodies [60–64]. The canonical form of the magnetic work per unit volume done to magnetize the polarizable medium, $\boldsymbol{H}\cdot\delta\boldsymbol{B}$, leads to the magnetic stress tensor

$$\mathcal{T}_m = -\frac{\mu_0}{2}H^2\mathcal{I} + \boldsymbol{B}\boldsymbol{H}. \tag{35}$$

The local effect of magnetic fields on the continuous magnetizable medium can be formulated in terms of both volume ($\boldsymbol{f}_m^V$) and surface ($\boldsymbol{f}_m^S$) magnetic force densities. The force per unit volume, or magnetic body force, is determined by the divergence of magnetic stress tensor

$$\boldsymbol{f}_m^V = \nabla\cdot\mathcal{T}_m = -\mu_0 H\nabla H + \nabla\cdot(\boldsymbol{B}\boldsymbol{H}), \tag{36}$$

By considering $\boldsymbol{B} = \mu_0(\boldsymbol{H}+\boldsymbol{M})$ as well as the solenoidal nature of the magnetic induction field ($\nabla\cdot\boldsymbol{B}=0$), the dyadic product $\boldsymbol{B}\boldsymbol{H}$ becomes

$$\nabla\cdot(\boldsymbol{B}\boldsymbol{H}) = (\boldsymbol{B}\cdot\nabla)\boldsymbol{H} = \mu_0(\boldsymbol{H}\cdot\nabla)\boldsymbol{H} + \mu_0(\boldsymbol{M}\cdot\nabla)\boldsymbol{H}. \tag{37}$$

When this expression is substituted in Eq. (36), and taking into account the general result

$$H\nabla H = (\boldsymbol{H}\cdot\nabla)\boldsymbol{H} + \boldsymbol{H}\times(\nabla\times\boldsymbol{H}), \tag{38}$$

the general expression

$$\boldsymbol{f}_m^V = -\mu_0\boldsymbol{H}\times(\nabla\times\boldsymbol{H}) + \mu_0(\boldsymbol{M}\cdot\nabla)\boldsymbol{H} \tag{39}$$

is derived [3].

In the problem of interest, no electric current are applied to the involved magnetic media. Therefore, $\boldsymbol{H}$ is an irrotational field. On the other hand, the constitutive relation that is assumed for these media implies that the fields $\boldsymbol{M}$ and $\boldsymbol{H}$ are aligned, so that $\boldsymbol{M} = (M/H)\boldsymbol{H}$. If both conditions (together with Eq. (38)) are taken into account in the above general expression, the relations

$$\boldsymbol{f}_m^V = \mu_0(\boldsymbol{M}\cdot\nabla)\boldsymbol{H} = \mu_0 M\nabla H \tag{40}$$

are finally obtained. The equivalence between the above expressions for the Kelvin force of Eq. (40) is due to the collinearity that is assumed for the fields $\boldsymbol{M}$ and $\boldsymbol{H}$, regardless of the characteristic constitutive relationship of the medium, $M/H = \chi_m(H)$.

In the case under study of axisymmetric magnetic fields whose azimuthal component is null and that only depend on the cylindrical coordinates r and z, the Kelvin force is $\boldsymbol{f}_m^V = f_r\boldsymbol{e}_r + f_z\boldsymbol{e}_z$, with

$$f_r = \mu_0\left(M_r\frac{\partial H_r}{\partial r} + M_z\frac{\partial H_r}{\partial z}\right), \tag{41a}$$

$$f_z = \mu_0\left(M_r\frac{\partial H_z}{\partial r} + M_z\frac{\partial H_z}{\partial z}\right), \tag{41b}$$

being the corresponding components of the magnetic force that appear in Eqs. (12b) and (12c), respectively. These expressions are directly obtained form $\mu_0(\boldsymbol{M}\cdot\nabla)\boldsymbol{H}$. The irrotationality of the field $\boldsymbol{H}$ implies $\partial H_r/\partial z = \partial H_z/\partial r$ which, applied in Eqs. 40 and (41), leads to the expression of the Kelvin force as $\mu_0(M\nabla H)$.

The imanation field $\boldsymbol{M}$ is discontinuous between the internal (∂V^-) and external (∂V^+) faces of the surface ∂V bounding the magnetized media, since $\boldsymbol{M}^+ = \boldsymbol{0}$ and $\boldsymbol{M}^- \neq \boldsymbol{0}$. In consequence, the magnetic stress tensor also has a discontinuity through ∂V, and a magnetic traction force arises at said interface [3,61,63,64], which is described by the surface density

$$\boldsymbol{f}_m^S = \boldsymbol{n}\cdot\mathcal{T}_m^+ - \boldsymbol{n}\cdot\mathcal{T}_m^-, \tag{42}$$

with

$$\boldsymbol{n}\cdot\mathcal{T}_m^\pm = -\frac{\mu_0}{2}\left(H^\pm\right)^2\boldsymbol{n} + B_n^\pm\boldsymbol{H}^\pm \tag{43}$$

and $\boldsymbol{n}$ being the external normal vector at ∂V. According to Gauss's law, the normal component of the induction field is continuous through ∂V ($B_n^+ = B_n^- = B_n$). In addition, the absence of electrical surface currents in ∂V results in the continuity of the tangential magnetic field component ($H_t^+ = H_t^- = H_t$). Therefore, Eq. (42) becomes

$$\boldsymbol{f}_m^S = -\frac{\mu_0}{2}\left[\left(H_n^+\right)^2 - \left(H_n^-\right)^2\right]\boldsymbol{n} + B_n\left(H_n^+ - H_n^-\right)\,\boldsymbol{n}. \tag{44}$$

Using the definition of the magnetic field $\boldsymbol{H}$ on the external and internal faces of ∂V,

$$H_n^+ = \frac{B_n}{\mu_0};\quad H_n^- = \frac{B_n}{\mu_0} - M_n^- \tag{45}$$

the result for the surface distribution of magnetic force at ∂V is

$$\boldsymbol{f}_m^S = \frac{\mu_0}{2}\left(M_n^-\right)^2\boldsymbol{n}. \tag{46}$$

It should be noted that this surface magnetic force density, normal to ∂V, corresponds to the magnetic traction term p_n in Eqs. (8a) and (22a).

Appendix B. Finite differences framework

The governing equations of the problem are discretized in the uniform $s-\eta$ computational grids. The first and second fourth-order derivatives of each variable f are computed as

$$\frac{\partial^n f}{\partial x^n}(x_0) = \frac{1}{12\Delta x^n}\sum_{i=-4}^{4}[c_i f(x_i)] + O(\Delta x^4), \tag{47}$$

with x_i being the spatial coordinate (s or η) at node i and $i=0$ the node under consideration, Δx the uniform grid space, $f(x_i)$ the value of the variable at x_i, c_i a coefficient given by Table 6, and n the order of the derivative. Forward, central, and backward finite differences are implemented depending on whether the node is located in the boundary or bulk of the domain.

Second-order backward finite differences are employed in the time domain using a fixed time step Δt, resulting in

$$\frac{\partial f}{\partial t} = \frac{1}{2\Delta t}[3f(t_0) - 4f(t_{-1}) + f(t_{-2})] + O(\Delta t^2), \tag{48}$$

where t_0 denotes the time under consideration. The first time step is computed with a first-order approximation of the derivative assuming an initial steady state.

Table 6
Fourth-order finite difference coefficients.

Type	Order	c_{-4}	c_{-3}	c_{-2}	c_{-1}	c_0	c_1	c_2	c_3	c_4
Forward 1	1					-25/12	4	-3	4/3	-1/4
	2					35/12	-26/3	19/2	-14/3	11/12
Forward 2	1				-1/4	-5/6	3/2	-1/2	1/12	
	2				11/12	-5/3	1/2	1/3	-1/12	
Central	1			1/12	-2/3	0	2/3	-1/12		
	2			-1/12	4/3	-5/2	4/3	-1/12		
Backward $n-1$	1		-1/12	1/2	-3/2	5/6	1/4			
	2		-1/12	1/3	1/2	-5/3	11/12			
Backward n	1	1/4	-4/3	3	-4	25/12				
	2	11/12	-14/3	19/2	-26/3	35/12				

Appendix C. Magnetic Comsol multiphysics model

In order to verify the magnetic field and force from the simulation for a given meniscus profile and coils current intensity, the problem is reproduced in Comsol Multiphysics by solving the stationary Maxwell equations

$$\nabla \times \boldsymbol{H} = \boldsymbol{J}, \tag{49}$$

$$\boldsymbol{B} = \nabla \times \boldsymbol{A}, \tag{50}$$

$$\boldsymbol{J} = \overline{\sigma}\boldsymbol{E}, \tag{51}$$

where $\boldsymbol{J}$ is the current field, $\boldsymbol{A}$ is the magnetic vector potential produced by the current in the coil and the magnetized materials, $\overline{\sigma}$ is the conductivity of the coil, and $\boldsymbol{E}$ is the electric displacement field. The constitutive relation

$$\boldsymbol{B} = \mu_0\mu_r\boldsymbol{H}, \tag{52}$$

with μ_r being the relative permeability of the material, is applied to the aluminum plates ($\mu_r^{Al} = 1.000022$), surrounding air ($\mu_r^{air} = 1$) and copper coils ($\mu_r^{Cu} = 1$). Within the ferrofluid volume, the constitutive relation is defined by the magnetization curve $M = f(H)$ depicted in Fig. 5, that results in

$$\boldsymbol{B} = \mu_0\left(1 + \frac{f(H)}{H}\right)\boldsymbol{H}, \tag{53}$$

where H is the module of the magnetic field $\boldsymbol{H}$. The current field is computed through

$$\boldsymbol{J} = \frac{NI}{S}\boldsymbol{e}_\phi, \tag{54}$$

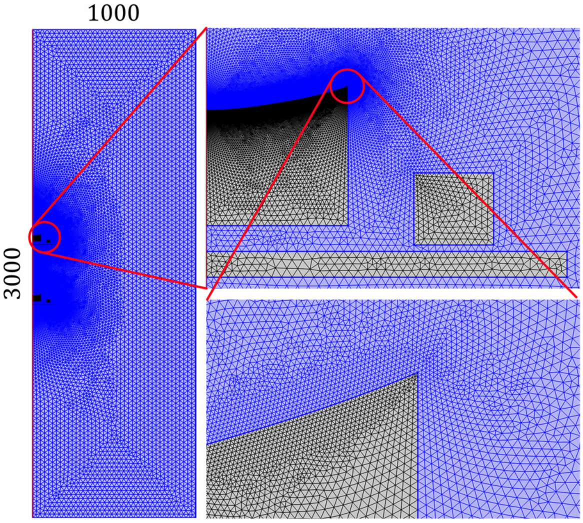

Fig. 18. Mesh employed by the magnetic Comsol Muliphysics model.

with $N = 200$ being the number of turns, I the current intensity flowing through each wire, $S = 509$ mm^2 the coils cross section and $\boldsymbol{e}_\phi$ the circumferential vector.

The simulation domain is a rectangular 1 × 3 m^2 region enclosing the assemblies. An axisymmetric boundary condition is applied to the symmetry axis, while the tangential magnetic potential is imposed at the external faces through $\boldsymbol{n} \times \boldsymbol{A} = \boldsymbol{n} \times \boldsymbol{A}_d$. $\boldsymbol{A}_d$ is the dipole term of the magnetic vector potential generated by the current in the coils and the magnetization fields of the ferrofluid volumes. Consequently, $\boldsymbol{A}_d$ is computed as the potential vector generated by four point dipoles applied at the centers of the magnetization distributions and whose moments are those of said distributions. While the dipoles associated to the coils can be calculated beforehand, the ferrofluid dipoles need to be approximated iteratively by integrating $\boldsymbol{M}$ in the ferrofluid volume. The relative error in the magnetic vector potential due the dipole approximation is estimated to be below 1.0% at the boundary of the domain with respect to the exact value generated by equivalent circular loops.

The mesh is composed of 167,755 irregular triangular elements, as shown in Fig. 18 for the $I = 20$ A case. Mean and minimum condition numbers of 0.985 and 0.527 are obtained. The governing equations are solved using Comsol's "Magnetic Fields" physics module with a stationary solver and a fully coupled implementation. The termination criterion set to "Solution or Residual" with a residual factor of 10^3.

References

[1] P. Poesio, E. Wang, Resonance induced wetting state transition of a ferrofluid droplet on superhydrophobic surfaces, Exp. Therm. Fluid Sci. 57 (2014) 353–357, doi:10.1016/j.expthermflusci.2014.02.012.

[2] H. Yamasaki, T. Kishimoto, T. Tazawa, H. Yamaguchi, Dynamic behavior of gas bubble detached from single orifice in magnetic fluid, J. Magn. Magn. Mater. 501 (2020) 166446, doi:10.1016/j.jmmm.2020.166446.

[3] A. Romero-Calvo, G. Cano-Gómez, T.H. Hermans, L. Parrilla Benítez, M. Herrada, E. Castro-Hernández, Total magnetic force on a ferrofluid droplet in microgravity, Exp. Therm. Fluid Sci. 117 (2020) 110124, doi:10.1016/j.expthermflusci.2020.110124.

[4] S.-H. Tan, N.-T. Nguyen, L. Yobas, T.G. Kang, Formation and manipulation of ferrofluid droplets at a microfluidic T-junction, J. Micromech. Microeng. 20 (4) (2010) 045004, doi:10.1088/0960-1317/20/4/045004.

[5] Y. Wu, T. Fu, Y. Ma, H.Z. Li, Active control of ferrofluid droplet breakup dynamics in a microfluidic t-junction, Microfluid. Nanofluid. 18 (1) (2015) 19–27, doi:10.1007/s10404-014-1414-y.

[6] M. Aboutalebi, M.A. Bijarchi, M.B. Shafii, S. Kazemzadeh Hannani, Numerical investigation on splitting of ferrofluid microdroplets in t-junctions using an asymmetric magnetic field with proposed correlation, J. Magn. Magn. Mater. 447 (2018) 139–149, doi:10.1016/j.jmmm.2017.09.053.

[7] J.C. Boulware, H. Ban, S. Jensen, S. Wassom, Experimental studies of the pressures generated by a liquid oxygen slug in a magnetic field, J. Magn. Magn. Mater. 322 (13) (2010) 1752–1757, doi:10.1016/j.jmmm.2009.12.022.

[8] A. Rosa, R. Gontijo, F. Cunha, Laminar pipe flow with drag reduction induced by a magnetic field gradient, Appl. Math. Model. 40 (5) (2016) 3907–3918, doi:10.1016/j.apm.2015.10.050.

[9] K. Kinefuchi, H. Kobayashi, Theoretical and experimental study of the active control of bubble point pressure using a magnetic field and its applications, Phys. Fluids 30 (6) (2018) 062101, doi:10.1063/1.5034222.

[10] A. Causevica, P. Sahli, F. Hild, K. Grunwald, M. Ehresmann, G. Herdrich, PAPELL: interaction study of ferrofluid with electromagnets of an experiment on the international space station, in: Proceedings of the 69th International Astronautical Congress, 2018, pp. 1–5.

[11] Y.Z. Sinzato, F.R. Cunha, Stability analysis of an interface between immiscible liquids in hele-shaw flow in the presence of a magnetic field, Appl. Math. Model. 75 (2019) 572–588, doi:10.1016/j.apm.2019.05.049.

[12] D. Ludovisi, S.S. Cha, N. Ramachandran, W.M. Worek, Heat transfer of thermocapillary convection in a two-layered fluid system under the influence of magnetic field, Acta Astronaut. 64 (11) (2009) 1066–1079, doi:10.1016/j.actaastro.2009.01.018.

[13] A. Bozhko, G. Putin, Thermomagnetic convection as a tool for heat and mass transfer control in nanosize materials under microgravity conditions, Microgravity Sci. Technol. 21 (1) (2009) 89–93, doi:10.1007/s12217-008-9059-7.

[14] B.A. Jackson, K.J. Terhune, L.B. King, Ionic liquid ferrofluid interface deformation and spray onset under electric and magnetic stresses, Phys. Fluids 29 (6) (2017) 064105, doi:10.1063/1.4985141.

[15] K. Lemmer, Propulsion for cubesats, Acta Astronaut. 134 (2017) 231–243, doi:10.1016/j.actaastro.2017.01.048.

[16] A. Bibo, R. Masana, A. King, G. Li, M. Daqaq, Electromagnetic ferrofluid-based energy harvester, Phys. Lett. A 376 (32) (2012) 2163–2166, doi:10.1016/j.physleta.2012.05.033.

[17] S.F. Alazemi, A. Bibo, M.F. Daqaq, A ferrofluid-based energy harvester: an experimental investigation involving internally-resonant sloshing modes, Eur. Phys. J. Spec. Top. 224 (14) (2015) 2993–3004, doi:10.1140/epjst/e2015-02602-9.

[18] S. Alazmi, Y. Xu, M.F. Daqaq, Harvesting energy from the sloshing motion of ferrofluids in an externally excited container: analytical modeling and experimental validation, Phys. Fluids 28 (7) (2016) 077101, doi:10.1063/1.4954787.

[19] C. Singh, A.K. Das, P.K. Das, Flow restrictive and shear reducing effect of magnetization relaxation in ferrofluid cavity flow, Phys. Fluids 28 (8) (2016) 087103, doi:10.1063/1.4960085.

[20] A. Shafiei Dizaji, M. Mohammadpourfard, H. Aminfar, A numerical simulation of the water vapor bubble rising in ferrofluid by volume of fluid model in the presence of a magnetic field, J. Magn. Magn. Mater. 449 (2018) 185–196, doi:10.1016/j.jmmm.2017.10.010.

[21] K. Ling, K.-K. Guo, S. Zhang, W.-Q. Tao, A numerical investigation on dynamics of ferrofluid droplet in nonuniform magnetic field, Numer. Heat Transf. Part A 75 (10) (2019) 690–707, doi:10.1080/10407782.2019.1609277.

[22] A. Romero-Calvo, G. Cano Gómez, E. Castro-Hernández, F. Maggi, Free and forced oscillations of magnetic liquids under low-gravity conditions, J. Appl. Mech. 87 (2) (2020), doi:10.1115/1.4045620. 021010

[23] X. Li, Z.-Q. Dong, P. Yu, X.-D. Niu, L.-P. Wang, D.-C. Li, H. Yamaguchi, Numerical investigation of magnetic multiphase flows by the fractional-step-based multiphase lattice Boltzmann method, Phys. Fluids 32 (8) (2020) 083309, doi:10.1063/5.0020903.

[24] V.G.e. Abicalil, R.F. Abdo, L.H.P. da Cunha, T.F. de Oliveira, On the magnetization of dilute ferrofluid emulsions in shear flows, Phys. Fluids 33 (5) (2021) 053313, doi:10.1063/5.0050643.

[25] A. Khan, S.-T. Zhang, Q.-P. Li, H. Zhang, Y.-Q. Wang, X.-D. Niu, Wetting dynamics of a sessile ferrofluid droplet on solid substrates with different wettabilities, Phys. Fluids 33 (4) (2021) 042115, doi:10.1063/5.0047553.

[26] F. Selimefendigil, H.F. Öztop, Mixed convection of ferrofluids in a lid driven cavity with two rotating cylinders, Eng. Sci. Technol. Int. J. 18 (3) (2015) 439–451, doi:10.1016/j.jestch.2015.03.003.

[27] M. Sheikholeslami, M.M. Rashidi, Ferrofluid heat transfer treatment in the presence of variable magnetic field, Eur. Phys. J. Plus 130 (6) (2015) 115, doi:10.1140/epjp/i2015-15115-4.

[28] Q. Liu, S.F. Alazemi, M.F. Daqaq, G. Li, A ferrofluid based energy harvester: computational modeling, analysis, and experimental validation, J. Magn. Magn. Mater. 449 (2018) 105–118, doi:10.1016/j.jmmm.2017.09.064.

[29] M. Heil, A.L. Hazel, J. Boyle, Solvers for large-displacement fluid–structure interaction problems: segregated versus monolithic approaches, Comput. Mech. 43 (1) (2008) 91–101, doi:10.1007/s00466-008-0270-6.

[30] B. Markert, Y. Heider, W. Ehlers, Comparison of monolithic and splitting solution schemes for dynamic porous media problems, Int. J. Numer. Methods Eng. 82 (11) (2010) 1341–1383, doi:10.1002/nme.2789.

[31] U. Küttler, M. Gee, C. Förster, A. Comerford, W.A. Wall, Coupling strategies for biomedical fluid-structure interaction problems, Int. J. Numer. Method Biomed. Eng. 26 (3–4) (2010) 305–321, doi:10.1002/cnm.1281.

[32] M. Mayr, T. Klöppel, W.A. Wall, M.W. Gee, A temporal consistent monolithic approach to fluid-structure interaction enabling single field predictors, SIAM J. Sci. Comput. 37 (1) (2015) B30–B59, doi:10.1137/140953253.

[33] Y. Hu, D. Li, X. Niu, Phase-field-based lattice Boltzmann model for multiphase ferrofluid flows, Phys. Rev. E 98 (2018) 033301, doi:10.1103/PhysRevE.98.033301.

[34] Y. Huang, Y. Zhang, M. Xu, J. Lei, Z. Li, W. Ye, A numerical investigation of bubble dynamics in a ferrofluid by improved multicomponent multiphase pseudopotential lattice Boltzmann model coupled with magnetic field solver, Phys. Fluids 33 (9) (2021) 097110, doi:10.1063/5.0066572.

[35] C.-S. Zhu, Z. Hu, K.-M. Wang, Multi-bubble motion behavior of uniform magnetic field based on phase field model, Chin. Phys. B 29 (3) (2020) 034702, doi:10.1088/1674-1056/ab6839.

[36] S. Popinet, Numerical models of surface tension, Annu. Rev. Fluid Mech. 50 (1) (2018) 49–75, doi:10.1146/annurev-fluid-122316-045034.

[37] S. Mirjalili, S.S. Jain, M.S. Dodd, Interface-capturing methods for two-phase flows: an overview and recent developments, in: Annual Research Briefs, Center for Turbulence Research, Stanford University, 2017, pp. 117–135.

[38] M. Herrada, J. Montanero, A numerical method to study the dynamics of capillary fluid systems, J. Comput. Phys. 306 (2016) 137–147, doi:10.1016/j.jcp.2015.11.048.

[39] A. Romero-Calvo, T.H. Hermans, G.C. Gómez, L.P. Benítez, M.H. Gutiérrez, E. Castro-Hernández, Ferrofluid dynamics in microgravity conditions, in: Proceedings of the 2nd Symposium on Space Educational Activities, 2018, pp. 1–5. Budapest, Hungary

[40] A. Romero-Calvo, T.H. Hermans, L.P. Benítez, E. Castro-Hernández, Drop Your Thesis! 2017 Experiment Report - Ferrofluids Dynamics in Microgravity Conditions, European Space Agency - Erasmus Experiment Archive, 2018.

[41] Á. Romero-Calvo, M.Á. Herrada, T.H.J. Hermans, L.P. Benítez, G. Cano-Gómez, E. Castro-Hernández, Axisymmetric ferrofluid oscillations in a cylindrical tank in microgravity, Microgravity Sci. Technol. 33 (4) (2021) 50, doi:10.1007/s12217-021-09894-4.

[42] A. Romero-Calvo, A. García-Salcedo, F. Garrone, I. Rivoalen, G. Cano-Gómez, E. Castro-Hernández, M.H. Gutiérrez, F. Maggi, STELIUM: a student experiment to investigate the sloshing of magnetic liquids in microgravity, Acta Astronaut. 173 (2020) 344–355, doi:10.1016/j.actaastro.2020.04.013.

[43] A. Romero-Calvo, A. García-Salcedo, F. Garrone, I. Rivoalen, G. Cano-Gómez, E. Castro-Hernández, F. Maggi, Free surface reconstruction of opaque liquids in microgravity, Part 1: design and on-ground testing, Acta Astronaut. 189 (2021) 250–259, doi:10.1016/j.actaastro.2021.08.029.

[44] A. Romero-Calvo, F. Garrone, A. García-Salcedo, I. Rivoalen, G. Cano-Gómez, E. Castro-Hernández, F. Maggi, Free surface reconstruction of opaque liquids in microgravity. Part 2: drop tower campaign, Acta Astronaut. 189 (2021) 269–277, doi:10.1016/j.actaastro.2021.07.020.

[45] A. Romero-Calvo, A.J. García-Salcedo, F. Garrone, I. Rivoalen, F. Maggi, Lateral and axisymmetric ferrofluid oscillations in a cylindrical tank in microgravity, AIAA J. 60 (4) (2022) 2707–2712, doi:10.2514/1.J061351.

[46] W.C. Reynolds, H.M. Satterlee, Ch. 11 - liquid propellant behavior at low and zero g, in: The Dynamic Behavior of Liquids in Moving Containers, NASA SP-106, 1966, pp. 387–440.

[47] A. Myshkis, V. Babskii, N. Kopachevskii, L. Slobozhanin, A. Tyuptsov, Low-Gravity Fluid Mechanics: Mathematical Theory of Capillary Phenomena, Springer, 1987.

[48] R. Hung, H. Pan, Mathematical model of bubble sloshing dynamics for cryogenic liquid helium in orbital spacecraft dewar container, Appl. Math. Model. 19 (8) (1995) 483–498, doi:10.1016/0307-904X(95)00033-G.

[49] S. Papell, Low Viscosity Magnetic Fluid Obtained by the Colloidal Suspension of Magnetic particles, US Patent 3215572, 1963.

[50] J. Martin, J. Holt, Magnetically Actuated Propellant Orientation Experiment, Controlling Fluid Motion with Magnetic Fields in a Low-Gravity Environment, NASA/TM-2000-210129, M-975, NAS 1.15:210129, 2000.

[51] J. Hochstein, J. R. Warren, J. George Schmidt, J. Hochstein, J. R. Warren, J. George Schmidt, Magnetically actuated propellant orientation (MAPO) experiment - pre-flight flow field predictions, in: 35th Aerospace Sciences Meeting and Exhibit, 1997, pp. 1–11, doi:10.2514/6.1997-570. AIAA Paper 1997-570

[52] J. Marchetta, J. Hochstein, Fluid capture by a permanent ring magnet in reduced gravity, in: Proceedings of the 37th Aerospace Sciences Meeting and Exhibit, Reno, NV, USA, American Institute of Aeronautics and Astronautics, 1999, pp. 1–14, doi:10.2514/6.1999-845. AIAA Paper 1999-845

[53] J. Marchetta, J. Hochstein, Simulation and dimensionless modeling of magnetically induced reorientation, in: Proceedings of the 38th Aerospace Sciences Meeting and Exhibit, American Institute of Aeronautics and Astronautics, Reno, NV, USA, 2000, pp. 1–13, doi:10.2514/6.2000-700. AIAA Paper 2000-700

[54] J. Marchetta, J. Hochstein, D. Sauter, B. Simmons, Modeling and prediction of magnetic storage and reorientation of lox in reduced gravity, in: 40th AIAA Aerospace Sciences Meeting & Exhibit, American Institute of Aeronautics and Astronautics, 2002, pp. 1–19, doi:10.2514/6.2002-1005. AIAA Paper 2002-1005

[55] J.G. Marchetta, Simulation of LOX reorientation using magnetic positive positioning, Microgravity Sci. Technol. 18 (1) (2006) 31, doi:10.1007/BF02908417.

[56] J. Marchetta, K. Roos, A three-dimensional computational simulation of magnetic positive positioning, in: 45th AIAA Aerospace Sciences Meeting and Exhibit, 2007, pp. 1–11, doi:10.2514/6.2007-956. AIAA Paper 2007-956

[57] J. Marchetta, K. Roos, Simulating magnetic positive positioning of liquids in a transient acceleration field, in: 46th AIAA Aerospace Sciences Meeting and Exhibit, 2007, pp. 1–11, doi:10.2514/6.2008-820. AIAA Paper 2008-820

[58] J.G. Marchetta, B.D. Simmons, J.I. Hochstein, Magnetic retention of LO2 in an accelerating environment, Acta Astronaut. 62 (8) (2008) 478–490, doi:10.1016/j.actaastro.2008.01.016.

[59] J. Marchetta, A. Winter, Simulation of magnetic positive positioning for space based fluid management systems, Math. Comput. Model. 51 (9) (2010) 1202–1212, doi:10.1016/j.mcm.2010.01.002.

[60] L. Landau, E. Lifshitz, Electrodynamics of Continuous Media, Pergamon Press, 1960.

[61] A. Engel, R. Friedrichs, On the electromagnetic force on a polarizable body, Am. J. Phys. 70 (4) (2002) 428–432, doi:10.1119/1.1432971.

[62] R.E. Rosensweig, Continuum equations for magnetic and dielectric fluids with internal rotations, J. Chem. Phys. 121 (3) (2004) 1228–1242, doi:10.1063/1.1755660.

[63] R.E. Rosensweig, Stress boundary-conditions in ferrohydrodynamics, Ind. Eng. Chem. Res. 46 (19) (2007) 6113–6117, doi:10.1021/ie060657e.

[64] R.E. Rosensweig, Ferrohydrodynamics, Dover Publications, 1997.

[65] J.D. Jackson, Classical Electrodynamics, third ed., Wiley, New York, NY, 1999.

[66] A. Romero-Calvo, M. Herrada, G. Cano-Gómez, H. Schaub, Advanced numerical simulation of magnetic liquid sloshing in microgravity, in: Proceedings of the 71st International Astronautical Congress, The CyberSpace Edition, 2020, pp. 1–8.

[67] Y. Dimakopoulos, J. Tsamopoulos, A quasi-elliptic transformation for moving boundary problems with large anisotropic deformations, J. Comput. Phys. 192 (2) (2003) 494–522, doi:10.1016/j.jcp.2003.07.027.

[68] A. Romero-Calvo, F. Maggi, H. Schaub, Magnetic positive positioning: toward the application in space propulsion, Acta Astronaut. 187 (2021) 348–361, doi:10.1016/j.actaastro.2021.06.045.

[69] D.T. Operation, S. Company, ZARM Drop Tower User Manual, ZARM FABmbH, 2011.

[70] G. Yeh, Free and forced oscillations of a liquid in an axisymmetric tank at low-gravity environments, J. Appl. Mech. 34 (1) (1967) 23–28, doi:10.1115/1.3607644.

[71] J. Gerstmann, M.E. Dreyer, Axisymmetric surface oscillations in a cylindrical container with compensated gravity, Ann. N. Y. Acad. Sci. 1077 (1) (2006) 328–350, doi:10.1196/annals.1362.022.

[72] B.M. Berkovsky, N.N. Smirnov, Capillary hydrodynamic effects in high magnetic fields, J. Fluid Mech. 187 (1988) 319–327, doi:10.1017/S0022112088000448.

[73] M. Shliomis, Effective viscosity of magnetic suspensions, Soviet Phys. JETP 34 (1972) 1291–1294.

[74] J.A. Nicolás, J.M. Vega, A note on the effect of surface contamination in water wave damping, J. Fluid Mech. 410 (2000) 367–373, doi:10.1017/S002211209900823X.

[75] M. Herrada, J. Montanero, J. Vega, The effect of surface shear viscosity on the damping of oscillations in millimetric liquid bridges, Phys. Fluids 23 (8) (2011), doi:10.1063/1.3623425.

[76] P. Lin, X. Lin, L.E. Johns, R. Narayanan, Stability of a static liquid bridge knowing only its shape, Phys. Rev. Fluids 4 (2019) 123904, doi:10.1103/PhysRevFluids.4.123904.

[77] R.M. Jenson, A.P. Wollman, M.M. Weislogel, L. Sharp, R. Green, P.J. Canfield, J. Klatte, M.E. Dreyer, Passive phase separation of microgravity bubbly flows using conduit geometry, Int. J. Multiphase Flow 65 (2014) 68–81, doi:10.1016/j.ijmultiphaseflow.2014.05.011.

[78] N.C. White, S.M. Troian, Why capillary flows in slender triangular grooves are so stable against disturbances, Phys. Rev. Fluids 4 (2019) 054003, doi:10.1103/PhysRevFluids.4.054003.

[79] F. Dodge, The New Dynamic Behavior of Liquids in Moving Containers, Southwest Research Institute, 2000.